



# The Isaac Newton Telescope Monitoring Survey of Local Group Dwarf Galaxies. VI. The Star Formation History and Dust Production in Andromeda IX

Hedieh Abdollahi<sup>1</sup> , Atefeh Javadi<sup>2</sup> , Mohammad Taghi Mirtorabi<sup>1,3</sup> , Elham Saremi<sup>2,4,5</sup> , Jacco Th. van Loon<sup>6</sup> ,  
Habib G. Khosroshahi<sup>2,7</sup> , Iain McDonald<sup>8,9</sup> , Elahe Khalouei<sup>2</sup> , Hamidreza Mahani<sup>2</sup>, Sima Taefi Aghdam<sup>2</sup>,  
Maryam Saberi<sup>10,11</sup> , and Maryam Toriki<sup>2</sup>

<sup>1</sup> Physics Department, Faculty of Physics and Chemistry, Alzahra University, Vanak, 1993891176, Tehran, Iran

<sup>2</sup> School of Astronomy, Institute for Research in Fundamental Sciences (IPM), P.O. Box 19395-5531, Tehran, Iran; [atefeh@ipm.ir](mailto:atefeh@ipm.ir)

<sup>3</sup> ICRA Net, Piazza della Repubblica 10, I-65122 Pescara, Italy

<sup>4</sup> Instituto de Astrofísica de Canarias, Vía Láctea s/n, E-38205 La Laguna, Tenerife, Spain

<sup>5</sup> Departamento de Astrofísica, Universidad de La Laguna, E-38205 La Laguna, Tenerife, Spain

<sup>6</sup> Lennard-Jones Laboratories, Keele University, ST5 5BG, UK

<sup>7</sup> Iranian National Observatory, Institute for Research in Fundamental Sciences (IPM), Tehran, Iran

<sup>8</sup> Jodrell Bank Centre for Astrophysics, Alan Turing Building, University of Manchester, Manchester, M13 9PL, UK

<sup>9</sup> Department of Physical Sciences, The Open University, Walton Hall, Milton Keynes, MK7 6AA, UK

<sup>10</sup> Roseland Centre for Solar Physics, University of Oslo, P.O. Box 1029 Blindern, NO-0315 Oslo, Norway

<sup>11</sup> Institute of Theoretical Astrophysics, University of Oslo, P.O. Box 1029 Blindern, NO-0315 Oslo, Norway

Received 2023 January 1; revised 2023 February 9; accepted 2023 February 12; published 2023 May 8

## Abstract

We present a photometric study of the resolved stellar populations in Andromeda IX (And IX), the closest satellite to M31, a metal-poor and low-mass dwarf spheroidal galaxy. We estimate a distance modulus of  $24.56_{-0.15}^{+0.05}$  mag based on the tip of the red giant branch. By probing the variability of asymptotic giant branch stars, we study the star formation history of And IX. We identified 50 long-period variables (LPVs) in And IX using the Isaac Newton Telescope in two filters, the Sloan  $i'$  and Harris  $V$ . In this study, we selected LPVs within two half-light radii with amplitudes in the range of 0.2–2.20 mag. It is found that the peak of star formation reaches  $\sim 8.2 \pm 3.1 \times 10^{-4} M_{\odot} \text{ yr}^{-1}$  at  $\approx 6$  Gyr ago. Our findings suggest an outside-in galaxy formation scenario for And IX with a quenching occurring  $3.65_{-0.13}^{+1.52}$  Gyr ago with a star formation rate (SFR) in the order of  $2.0 \times 10^{-4} M_{\odot} \text{ yr}^{-1}$  at redshift  $< 0.5$ . We calculate the total stellar mass by integrating the SFR within two half-light radii  $\sim 3.0 \times 10^5 M_{\odot}$ . By employing spectral energy distribution fitting for the observed LPVs in And IX, we evaluate a mass-loss rate in the range of  $10^{-7} \leq \dot{M} \leq 10^{-5} M_{\odot} \text{ yr}^{-1}$ . Finally, we show that the total mass deposition to the interstellar medium (ISM) is  $\sim 2.4 \times 10^{-4} M_{\odot} \text{ yr}^{-1}$  from the C- and O-rich types of dust-enshrouded LPVs. The ratio of the total mass returned to the ISM by LPVs to the total stellar mass is  $\sim 8.0 \times 10^{-10} \text{ yr}^{-1}$ , and so at this rate it would take  $\sim 1$  Gyr to reproduce this galaxy.

*Unified Astronomy Thesaurus concepts:* Local Group (929); Dwarf galaxies (416); Star formation (1569); Evolved stars (481); Asymptotic giant branch stars (2100); Stellar mass loss (1613); Dwarf spheroidal galaxies (420)

## 1. Introduction

Dwarf galaxies are the most abundant type of galaxy in the universe. They contain valuable information about the early universe and its evolution (Cignoni & Tosi 2010). Dwarf galaxies also continue to play an important role in our understanding of galaxy formation and stellar evolution (Tolstoy 2003). Dwarf galaxies are divided into two main categories based on their gas content: gas-rich dwarfs, such as dwarf irregulars (dIrrs) and blue compact dwarfs (BCDs), and gas-poor dwarfs, such as dwarf ellipticals (dEs), dwarf spheroidals (dSphs), and ultra-faint dwarfs (UFDs; Müller et al. 2021). The Local Group hosts various kinds of dwarf galaxies, and it is possible to study their resolved populations with space- or ground-based telescopes (Weisz et al. 2014).

Lambda cold dark matter ( $\Lambda$ CDM), which is known as the standard model of cosmology, is compatible with most observations. In  $\Lambda$ CDM, CDM is assumed to be the dominant matter content of the universe (Navarro 2018). In the

hierarchical  $\Lambda$ CDM paradigm, galaxies evolve in dark matter halos formed in the early universe by the gravitational collapse of overdense regions. Moreover, the halos grow hierarchically through the accretion of subhalos. The galaxies are surrounded by these subhalos, which are known as satellite galaxies (Shi et al. 2020).

One of the main challenges for the CDM scenario is the so-called missing satellite problem (Klypin et al. 1999; Del Popolo & Le Delliou 2017): there is a discrepancy between the number of satellites predicted in CDM simulations and the observed satellites. There is also another critical challenge, referred to as “Too Big To Fail.”  $N$ -body simulations, based on  $\Lambda$ CDM, predict that the satellites would be too massive and dense compared to those that are observed (Boylan-Kolchin et al. 2011, 2012; Del Popolo & Le Delliou 2017). Thus, further observation and study of dwarf galaxies may enable us to understand the universe and solve the aforementioned problems.

Several mechanisms (internal and external) could influence the evolution of dwarf galaxies. Compared to massive galaxies, dwarf galaxies have a smaller stellar population and a simple star formation history (SFH). There are internal processes, such as stellar feedback and depletion gas, and also environmental processes, such as tides and ram pressure stripping, that

influence star formation in dwarf galaxies (Gnedin 2014; Wetzel et al. 2015; Xu et al. 2016; Simpson et al. 2018; Fillingham et al. 2019; Wheeler et al. 2019; Applebaum et al. 2021).

An optical monitoring survey was initiated using the Isaac Newton Telescope (INT) to study the SFH of dwarf galaxies in the Local Group by probing asymptotic giant branch (AGB) stars (Saremi et al. 2020). Mass loss is one of the notable features of AGB stars with large-amplitude pulsations. These pulsations lead to long-period photometric variability that can be observed in durable photometric campaigns (Javadi et al. 2011a). The INT survey was launched to estimate the dust ejected into the interstellar medium (ISM) and to determine the mass-loss rate in 55 nearby galaxies, spanning an order of magnitude in metallicity. Long-period variables (LPVs) can be used to trace the stellar evolution and history of the galaxy. This survey allows us to compare the SFHs in different galaxy types and to study the evolution and quenching times of dwarf galaxies. We used a method introduced by Javadi et al. (2011b, 2017) to build the SFH of the galaxy M33 and to estimate the dust ejection into the ISM.

AGBs and red supergiants (RSGs) are powerful tools to study the SFH, as they have been present for most of the history of the universe ( $\sim 10$  Myr–10 Gyr) and are in their final stage of evolution, where their luminosity relates directly to their birth mass (Javadi et al. 2011b). Various surveys in the IR wavelength have widely studied AGBs and RSGs (Boyer et al. 2009; Javadi et al. 2011a; Battinelli & Demers 2013; Boyer et al. 2015a, 2015b; Javadi et al. 2015). Dust-producing LPVs are more easily detected in the optical bands because their amplitude is larger compared to the IR wavelength, though there has not yet been a comprehensive survey of LPV stars in Local Group dwarf galaxies. In addition, the inclusion of IR bands in spectral energy distributions (SEDs) makes the calculation of dust density more accurate, since the optical alone is not a sufficient indicator of dust density. The INT monitoring survey, thanks to a comprehensive sampling (to date), can address open questions about the evolution of dwarfs and shutting down of star formation by various effects such as environmental processes and tidal effects.

AGB stars can reach a luminosity of  $10^4 L_{\odot}$  (van Loon et al. 2005a) at their most luminous stage. These luminous populations are easily distinguished from the background, especially in the IR, where the difference in brightness is very pronounced. These types of stars are cool, with temperatures of  $\lesssim 4000$  K (van Loon et al. 2005a), and have a birth mass of  $0.8 M_{\odot} \leq M \leq 8 M_{\odot}$  (Höfner & Olofsson 2018). AGB stars consist of an electron-degenerate (C–O) core and two shells around it. Burning helium and hydrogen in the shells generates energy for evolution in AGBs. Helium shell burning releases considerable energy in a flash-like process, resulting in a long series of thermal pulses (Rosenfield et al. 2014). Periodic expansions and contractions of the outer layers lead to radial pulses, usually on the order of  $10^2$ – $10^3$  days (Höfner & Olofsson 2018). Most stars (especially AGBs) experience mass loss at the end of their evolution. Dust can be produced mainly in two environments: during the thermal-pulsation phase in the cool and dense atmosphere of AGBs with low-to-intermediate stellar mass ( $0.8$ – $8 M_{\odot}$ ), and during the core-collapse phase of stars with enough heavy mass ( $M > 8 M_{\odot}$ ) to end their lives with supernova explosions (Valiante et al. 2009). AGB stars deposit some of their mass into the ISM through radial mechanical pulsation and thus play a crucial role in enriching

**Table 1**  
Properties of the And IX Dwarf Galaxy

Parameter	Value	Reference
R.A. (J2000)	00 52 53	Zucker et al. (2004)
Decl. (J2000)	+43 11 45	Zucker et al. (2004)
$M_V$ (mag)	$-9.0 \pm 0.3$	Weisz et al. (2019a)
$r_h$ (pc)	$444_{-53}^{+68}$	Weisz et al. (2019a)
[Fe/H] (dex)	$-2.03 \pm 0.01$	Wojno et al. (2020)
$\sigma$ (km s $^{-1}$ ) <sup>a</sup>	$4.5_{-3.4}^{+3.6}$	Collins et al. (2010)
$\Sigma_V$ (mag arcsec $^{-2}$ ) <sup>b</sup>	$28.0 \pm 1.2$	McConnachie (2012)
$V$ (mag) <sup>c</sup>	$16.3 \pm 1.1$	Conn et al. (2012)

**Notes.**

<sup>a</sup> Observed velocity dispersion.

<sup>b</sup> Surface brightness.

<sup>c</sup> Apparent magnitude in the Vega magnitude system.

the ISM. van Loon et al. (1999) estimated a mass-loss rate in the range of  $10^{-7} < \dot{M} \leq 10^{-3} M_{\odot} \text{ yr}^{-1}$  based on a sample of AGBs and RSGs in the Large Magellanic Cloud (LMC).

In this paper, we focus on a spheroidal dwarf satellite along the major axis of the M31 galaxy, Andromeda IX (And IX), which is closest to the host and one of the least luminous satellites. And IX was discovered using the resolved stellar photometry of the Sloan Digital Sky Survey (SDSS) by Zucker et al. (2004) and categorized as an old dwarf galaxy with little baryonic matter. The classification of it being old was due to the fact that no significant populations of intermediate-age carbon and main-sequence stars were observed with the WIYN 3.5 m telescope by Harbeck et al. (2005). Table 1 shows in detail the apparent characteristics of And IX, which was selected for this study for the following reasons:

1. Studying one of the Andromeda satellites allows us to investigate whether the star-forming pattern and quenching time are consistent with those of the Milky Way. It also helps to understand whether this dwarf galaxy follows other M31 satellites in its formation scenario, as studied by Weisz et al. (2019b).
2. And IX is an important case study because of its proximity to the host,  $\sim 39_{-2}^{+5}$  kpc (Weisz et al. 2019a), in which quenching time and galaxy evolution may have been affected by environmental effects such as the strong tidal effect of M31.
3. With a mass-to-light ratio of  $1 M_{\odot}/L_{\odot}$ , McConnachie (2012) estimated the dynamical mass ( $6.5 \times 10^6 M_{\odot}$ ) and stellar mass ( $0.15 \times 10^6 M_{\odot}$ ), which could be a sign of the existence of large amounts of dark matter with a very low surface brightness of  $\Sigma_V = 28.0 \pm 1.2$  mag arcsec $^{-2}$ .

Different values have been reported for the distance modulus using two methods, the horizontal branch (HB) and the tip of the red giant branch (TRGB). In Table 2, we summarize the distance modulus calculated in other works. In this paper, we calculate a distance modulus of  $(m - M) = 24.56_{-0.15}^{+0.05}$  mag using the TRGB method (see Section 5).

This paper is organized as follows. In Section 2, we present the photometry results of And IX. Section 3 deals with the study of the variable candidates and their amplitudes. Cross-correlation of the INT catalog with the Spitzer, Wide-field Infrared Survey Explorer (WISE), and SDSS catalogs is discussed in Section 4. A description of the physical parameters of And IX is presented in Section 5. We focus on the estimation

**Table 2**  
Distance Modulus Reported in the Literature

Distance modulus (mag)	Method	Reference
$24.42 \pm 0.07$	TRGB	McConnachie et al. (2005)
$24.48 \pm 0.20$	TRGB	Zucker et al. (2004)
$24.33 \pm 0.10$	TRGB	Harbeck et al. (2005)
$24.42 \pm 0.39$	TRGB	Collins et al. (2010)
24.4	HB	Collins et al. (2010)
$24.46_{-0.15}^{+0.28}$	TRGB, HST <sup>a</sup>	Weisz et al. (2019a)
$24.43_{-0.03}^{+0.06}$	HB, HST <sup>b</sup>	Weisz et al. (2019a)
$23.89_{-0.08}^{+0.31}$	TRGB, Ground <sup>c</sup>	Weisz et al. (2019a)

**Notes.**

<sup>a</sup> Hubble Space Telescope (HST)-based TRGB distance modulus.

<sup>b</sup> HST-based HB distance modulus.

<sup>c</sup> Ground-based TRGB distance modulus.

of SFH based on the LPVs specifically in And IX in Section 6. Estimation of the mass-loss rate by modeling the SEDs based on the dust from LPVs is discussed in Section 7. Finally, a summary is presented in Section 8.

## 2. Photometry

Nine observations were made from 2015 June 21 to 2017 October 6 (Table 3), to determine the photometric variability of the stars. The observations were made with the 2.5 m Wide Field Camera (WFC) at INT in the Sloan  $i'$ , Harris  $V$ , and RGO  $I$  filters. The Sloan  $i'$  was used to observe the minimal effects of dust attenuation among the visible wavelengths in addition to the most significant magnitude differences of LPVs compared to other populations. The Harris  $V$  was also used to check the color, temperature, and radius. THE THELI (Transforming Heavenly Light into Image) pipeline was used to process each night's observations and create a comprehensive mosaic image by removing noise and tool errors (Saremi et al. 2020).

We performed photometric measurements of And IX using the DAOPHOT/ALLSTAR package (Stetson 1987) on a charge-coupled device (CCD). Because the CCD4 covered more than two half-light radii ( $\sim 5'$ ) of And IX, we focused our study on the CCD4 ( $11.26 \times 22.55$  arcmin<sup>2</sup>). DAOPHOT distinguished stars from background noise and measured stellar brightness by aperture photometry. To obtain a more accurate magnitude and astrometry, a point-spread function (PSF) was created by selecting a number of isolated and unsaturated stars in each image. The PSF-fitting photometry was performed with ALLSTAR by subtracting all stars in each image based on the constructed PSF model. DAOMASTER combined the output of ALLSTAR from multiple individual images. Individual images were combined to create a master mosaic image of the galaxy using MONTAGE2. Simultaneous reduction of all images by PSF-fitting photometry was performed by ALLFRAME (Stetson 1994). The master image from CCD4 with a half-light radius (yellow circle) and two half-light radii (blue circle) of And IX are shown in Figure 1. A total of 8653 stellar sources were detected in CCD4, of which  $\sim 4030$  are within the two half-light radius. The photometric calibrations were performed as follows:

1. Aperture correction: aperture growth curves were generated for a sample of stars ( $\sim 40$  bright and isolated stars) using the DAOGROW routine. The difference between the

**Table 3**  
Observations of And IX

Date (y m d)	Epoch	Filter	$t_{\text{exp}}$ (s)	Airmass
2015 06 21	1	$I$	45	1.265
2015 06 21	1	$V$	72	1.253
2016 02 09	2	$i$	540	1.854
2016 06 15	3	$i$	555	1.409
2016 08 11	4	$i$	555	1.045
2016 08 13	4	$V$	735	1.033
2016 10 21	5	$i$	555	1.320
2017 01 29	6	$i$	435	1.655
2017 08 01	7	$i$	555	1.306
2017 08 01	7	$V$	735	1.227
2017 09 02	8	$i$	555	1.070
2017 09 02	8	$V$	735	1.047
2017 10 06	9	$i$	555	1.341

PSF fitting and a large-aperture magnitude was derived from the COLLECT routine and added to all stellar sources using the NEWTRIAL routine (Stetson 1990, 1996).

2. Zero-point derivation: the transformation equations are derived by comparing Landolt standard stars and SDSS photometry based on the zero-point and atmospheric extinction (Jordi et al. 2006). The average of the zero points is used for nights without a standard field. The transformation equations are applied by the CCDAVE routine, and all images are calibrated with NEWTRIAL (Stetson 1996).
3. Relative calibration: we selected a sample of 1000 common stars in all images with magnitudes ranging from 17 to 21 mag. The mean magnitude was estimated at all epochs for each star, taking into account the photometric errors. We then applied the average value of the deviation of the mean magnitude of each star to all epochs. This step ensures that we have calibrated the magnitude of the LPVs. Fully described details of the photometric procedure can be found in Saremi et al. (2020).

To investigate photometric completeness, we performed the ADDSTAR task in the DAOPHOT package. A total of 1050 artificial stars in a range from 17 to 24 mag were added at random positions. The completeness limits as a function of magnitude are shown for long- and short-exposure-time images in the  $i$ ,  $I$ , and  $V$  bands in Figure 2. The completeness limit is at 100% above the peak of the RGB around  $\sim 21.20$  mag. The extracted catalog is more than 90% complete up to  $\sim 22$  mag for long-exposure frames and more than 85% complete in frames taken in 2015. The completeness limit as a criterion of recovered stars has dropped to 50% for fainter stars (magnitude  $> 22.8$  mag). The catalog covers all AGB stars in the observed region, as we search for AGB stars between the tip of the AGB at  $i = 17.29$  mag and the tip of the RGB at  $i = 21.20$  mag (see Section 5 for more information on how tips of the AGB and RGB are calculated). The magnitude differences between the recovered (output of photometry) and assigned magnitude (by ADDSTAR) of the artificial stars versus magnitude in the  $i$  band are shown in Figure 3. These differences range from  $-1 < \Delta i < 0.5$  mag. Despite the acceptable completeness in the  $I$ -band magnitude, we eliminated it in the later steps such as the search for variables and SFHs. The calibration procedures were not applied to this filter because there was no transformation equation between the

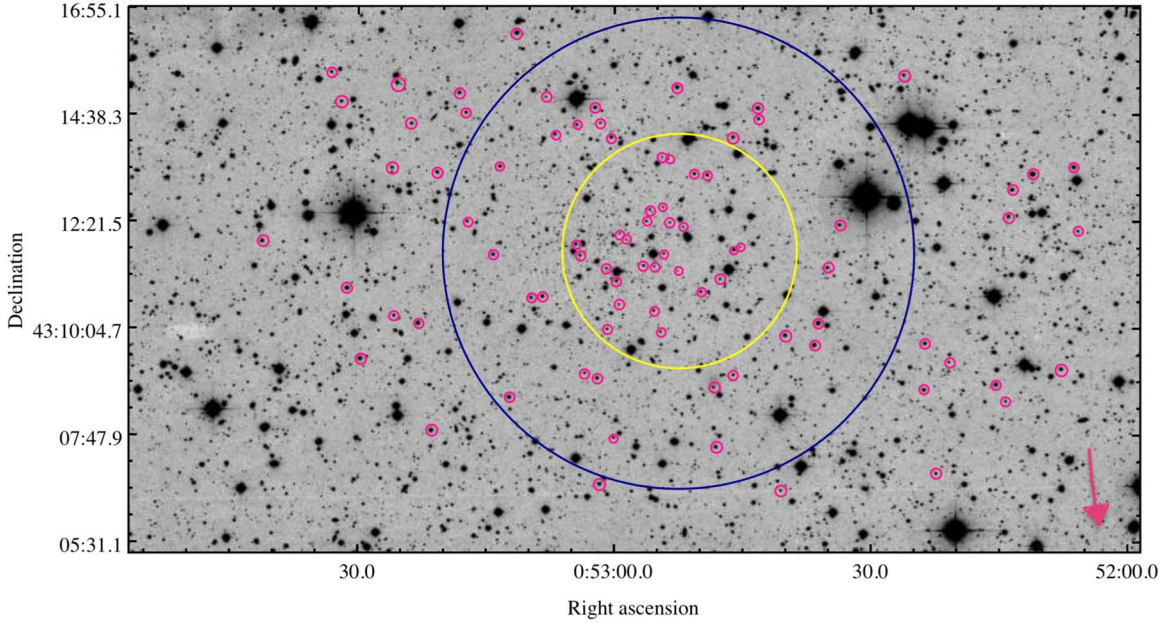


**Figure 1.** Montage of all frames of the And IX dSph galaxy with variable candidates in pink circles. Half-light radius of  $\sim 2/5$  (yellow circle) and two half-light radii (blue circle) of And IX are approximately noted. The pink arrow points toward the center of the M31 galaxy.

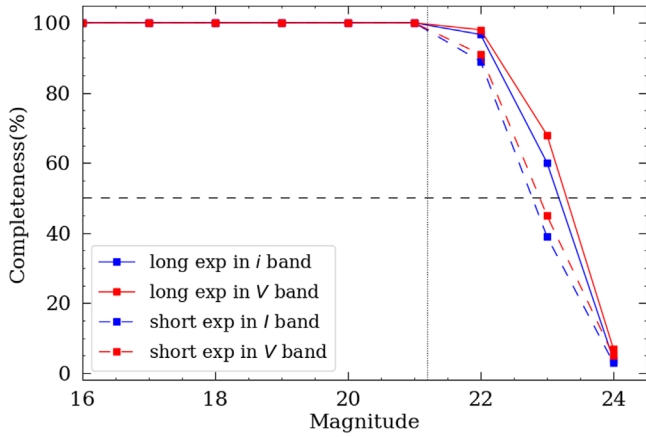


**Figure 2.** Completeness limit vs. magnitude for the long-exposure times in the *i* band (blue solid line) and in the *V* band (red solid line). The short-exposure times are also in the *i* band (blue dashed line) and *V* band (red dashed line). The dotted vertical line shows the tip of the RGB.

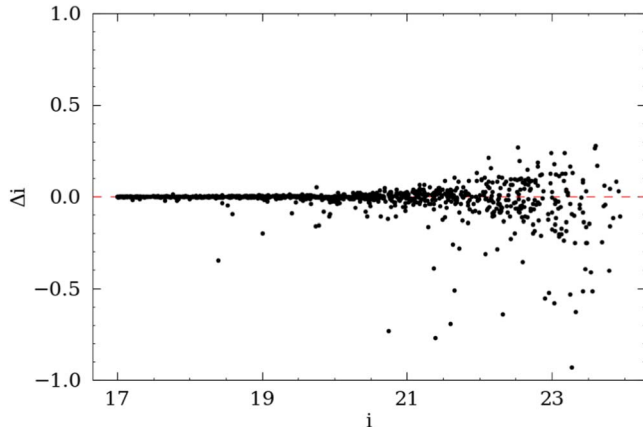


**Figure 3.** Differences between the recovered and assigned magnitudes of artificial stars by ADDSTAR vs. magnitude in the *i* band.

*I*-band magnitude and the two other bands (refer to Section 4.3 for more details).

### 3. Probing Variable Candidates

#### 3.1. Evaluation of Variables

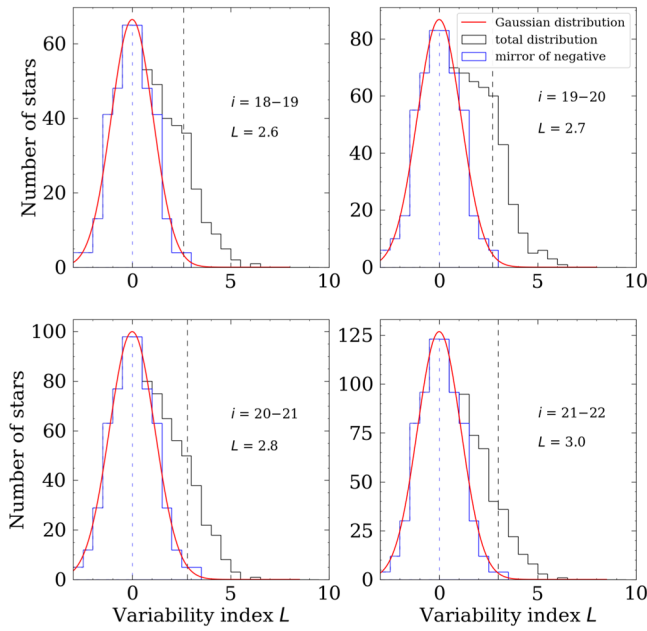
One of the most reliable methods for determining variability in a sample of stars was introduced by Welch & Stetson (1993), which was further developed in Stetson (1996). The decisive variable index, *L*, is determined by combining two indexes, *J* and *K*, as follows:

$$L = \frac{J \times K \sum_{i=1}^n \omega_i}{0.798 \omega_{\text{all}}}. \quad (1)$$

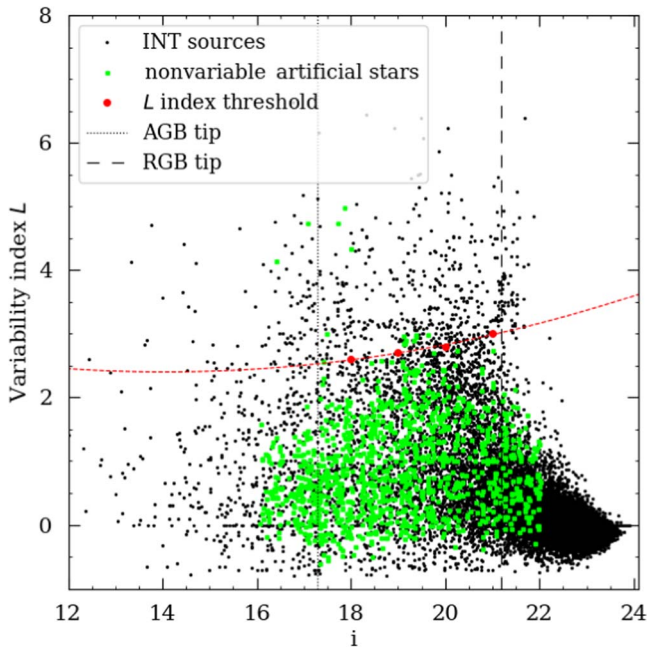
With random noise, the index *J* scatters around zero and has a large positive value for variable stars. The shape of the light curve is also influenced by the index *K*. If the time difference between two frames is closer than the period of variability, the weight of each star,  $\omega_i$ , is equal to 1, whereas in a single frame  $\omega_i = 0.5$ .  $\sum \omega_i$  is the total weight assigned to a star based on the number of detections and  $\omega_{\text{all}}$  is the total weight assigned to a star when it has been observed at all epochs.

Figure 4 can be considered as a Gaussian function (red curve), mirrored around  $L=0$ , with an excess at high *L*, representing statistically significant variable stars. We fit a Gaussian function to the negative distribution of *L* in each magnitude bin. If the number of stars in a given (positive) *L* and a given magnitude bin exceeds the Gaussian fit by a factor of 10 (indicating a 90% chance that it is a true variable), we set a threshold for candidate variability (vertical black dotted line). This threshold is indicated by the red dots in Figure 5.

Figure 5 shows a scatter plot of variability index *L* for different magnitude intervals. To detect variable candidates in all magnitude ranges, a polynomial function is fitted to the variability index threshold which varies with magnitude. A total of 411



**Figure 4.** The red curves are the predicted Gaussian functions fitted to histograms of the variability indexes of the And IX population. The blue dashed lines are with  $L = 0$  and the negative part of the blue histograms ( $L < 0$ ) are mirrored. The vertical black dashed lines represent the thresholds of the variability indexes in each magnitude bin.



**Figure 5.** Distribution of variability indexes as a function of magnitude with the best fit of the polynomial function (red dashed line) to the indexes threshold in  $i \in [18, 19, 20, 21]$  mag. Variability indexes of artificial stars in the range  $16 \leq i \leq 22$  mag are marked in green. The tips of the AGB and RGB are shown with vertical black lines at 17.29 and 21.20 mag, respectively.

variable candidates were detected over an area of about  $0.07 \text{ deg}^2$  ( $\sim$ area of CCD4).

The accuracy of the variability index estimate was evaluated using the ADDSTAR task in the DAOPHOT package (Stetson 1987). In this way, 1200 artificial stars with magnitudes in the range of 16–22 mag were added to all frames in six steps with random positions and constant light curves. Photometric procedures and assessment of variability index  $L$  for the synthetic population were

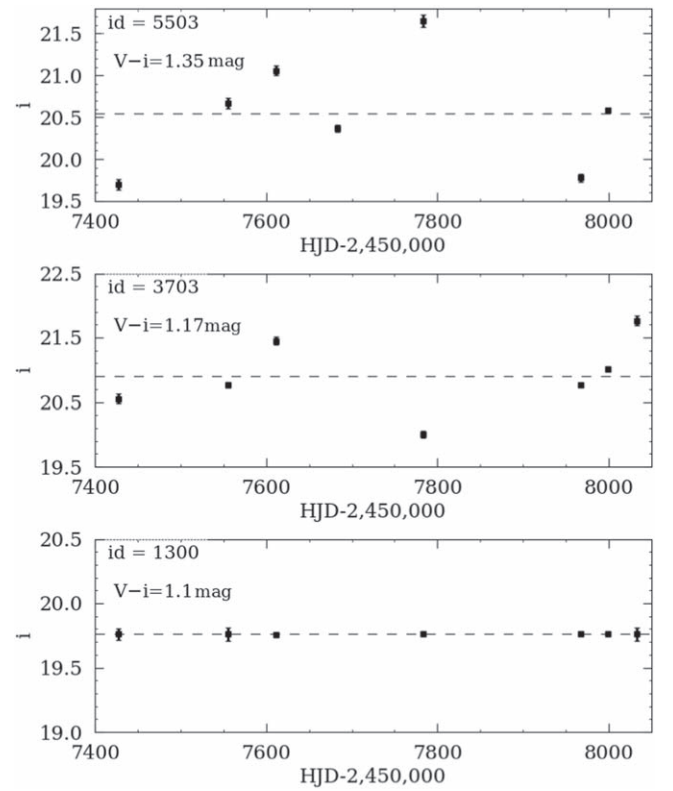


**Figure 6.** Examples of light curves, two variable candidates in the first two plots, and a nonvariable star in the third plot. Vertical error bars represent magnitude error.

performed as previously described. The distribution of the variability indexes of the artificial stars, based on their magnitude, is overplotted in Figure 5. It can be seen that no more than 1.16% of these artificial constant stars have a variability index above the threshold value, indicating a fairly reliable estimate of the threshold value.

Figure 6 shows the light curves of the variable candidates and a nonvariable star to highlight the distinction between their light curves. The magnitudes of the variable ones show remarkable changes around the mean magnitude (the first two plots), while the nonvariable star (the third plot) shows only small changes in magnitude around its mean, shown by horizontal dashed lines. Variable candidates (the first two plots) were detected in Spitzer and SDSS surveys (Planck Collaboration et al. 2014; Boyer et al. 2015a). In addition to these surveys, WISE also discovered candidate #5503 (Cutri et al. 2021). Table A1 provides more details about variable stars.

### 3.2. And IX Contamination

Foreground Milky Way contamination must be removed from And IX to distinguish dwarf-galaxy stellar populations, especially before SFHs are constructed from the LPVs. To detect foreground contamination, we cross-correlated our catalog with Gaia Data Release 3 (DR3; Gaia Collaboration et al. 2021). We also considered TRILEGAL simulations of the Milky Way population to account for the level of contamination (Girardi et al. 2005). The Gaia sources, in green, are overplotted on the INT populations in the upper panels of Figure 7. We included the entire field observed in CCD4 ( $0.07 \text{ deg}^2$ ; left panels of Figure 7) and a region within a half-light radius ( $0.005 \text{ deg}^2$ ; right panels of Figure 7). Populations of the Milky Way must either satisfy the

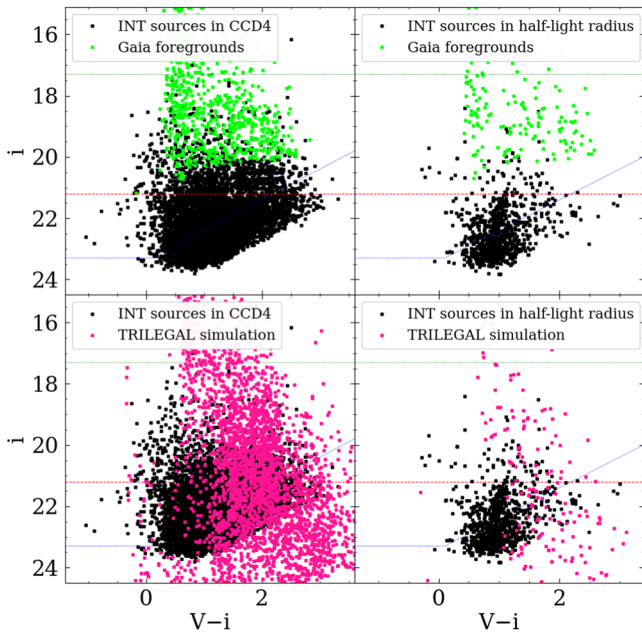


**Figure 7.** Gaia sources (in green) and TRILEGAL simulation of foreground contamination (in pink) presented as a function of color. The stellar population is confined in a field of  $\sim 0.07 \text{ deg}^2$  (area of CCD4) in the left panels, and in  $\sim 0.005 \text{ deg}^2$ , corresponding to the half-light radius, in the right panels. Tips of the AGB and RGB are marked in green and red dashed lines, respectively. The completeness limit of our photometry is marked in blue.

proper-motion criteria  $\sqrt{(\mu_{R.A.})^2 + (\mu_{Decl.})^2} > 0.28 \text{ c mas yr}^{-1} + 2.0 \text{ error for } \mu$  as proper motion or a parallax-error criterion  $\text{Pa}/(\text{error of Pa}) \geq 2\sigma$  (with Pa taken as parallax) (Saremi et al. 2020). Based on the adopted criteria, the total number of Gaia sources detected in our observation is estimated to be 890 in the region of CCD4 and 171 within the half-light radius of And IX. About 80% of the variable candidates in CCD4,  $\sim 55\%$  in two half-light radii and less than 27% within the half-light radius, are detected by Gaia as foreground contamination. Gaia’s faint-source limit is  $G \sim 20.5 \text{ mag}$  and its completeness limit is  $G \sim 17 \text{ mag}$  (Gaia Collaboration et al. 2021).

Foreground contamination of And IX is simulated using the TRILEGAL tool, at Galactic coordinates  $\ell = 123^\circ 212$ ,  $b = -19^\circ 675$ , and Galactic extinction  $A_V = 0.206 \text{ mag}$ . The stellar population predicted by TRILEGAL along the line of sight of And IX in two panels is shown in pink in the lower panels of Figure 7. There are 1990 synthetic stars predicted by TRILEGAL in CCD4 and 190 within the half-light radius. There is additional foreground contamination from the TRILEGAL simulation within CCD4 and the half-light radius compared to Gaia DR3 due to Gaia’s limitation in the detection of very faint stars ( $\sim i = 20.5 \text{ mag}$ ). Comparing the foreground contamination in the two regions in Figure 7, we see that foreground stars have less impact on the half-light radius despite a large number of foreground stars in CCD4.

In addition to the foreground stars of the Milky Way, our sample could be contaminated by stars in the halo of M31 (due to And IX’s proximity to M31). A plausible contamination by a giant stellar stream in the northeast of M31 has been suggested based on a study of velocity dispersion in the SPLASH survey (Tollerud et al. 2012). In addition, And IX is located in a halo substructure known as the Triangulum–Andromeda (TriAnd) region, and stars in this region could represent possible contamination (Rocha-Pinto et al. 2004).

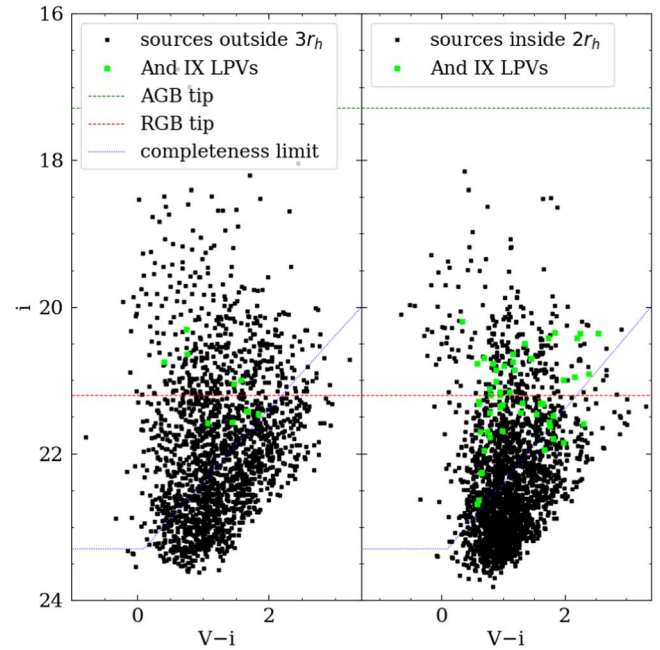


**Figure 8.** Color–magnitude diagrams (CMDs) of And IX in the  $i$  vs.  $V-i$  color showing our identified LPV candidates, in green, for two regions of a similar area within two half-light radii (right panel) and outside three half-light radii (left panel).

The distribution of LPVs as a function of color ( $V-i$ ) is compared in two regions with the same area to reveal the degree of contamination by the M31 halo in Figure 8. Contamination is estimated by comparing the population within two half-light radii (right panel) and outside of the three half-light radii (left panel). About 28% of the stellar population and 13% of the LPV candidates within two half-light radii are estimated as background contamination. Possibly they are stars in M31 and/or background active galactic nuclei (AGNs) and/or foregrounds that are below Gaia’s limit of completeness. Figure 8 (left panel), shows no clear, curved RGB in the control field, suggesting that M31 contamination is negligible and most of the contamination comes from the Galactic foreground. It is noted that background galaxies and AGN contamination mainly affect the regions around  $V-i \sim 2 \text{ mag}$  and  $i \gtrsim 21.5 \text{ mag}$ , not much affecting the AGB (or RGB) portion of the And IX color–magnitude diagram (CMD). In the following, foreground contamination of Gaia is excluded from the And IX population.

### 3.3. Amplitude of Variable Candidates

The shape of the light curve is assumed to be sinusoidal to evaluate the amplitude of variability. The light curves of the variable candidates in Figure 6 are considered as examples in our data that show sinusoidal variability due to pulsations (blue signs in Figure 9). Considering a value of 0.707 for the standard deviation of the unit sine function and a standard deviation in our data,  $\sigma$  (Javadi et al. 2011a), the amplitude is estimated by

$$\text{Amplitude} = \frac{2 \times \sigma}{0.707}. \quad (2)$$

The amplitude of the variable candidates in the range 0.1–2.20 mag, as a function of magnitude in the  $i$  band, is shown in the left panel of Figure 9. The horizontal black

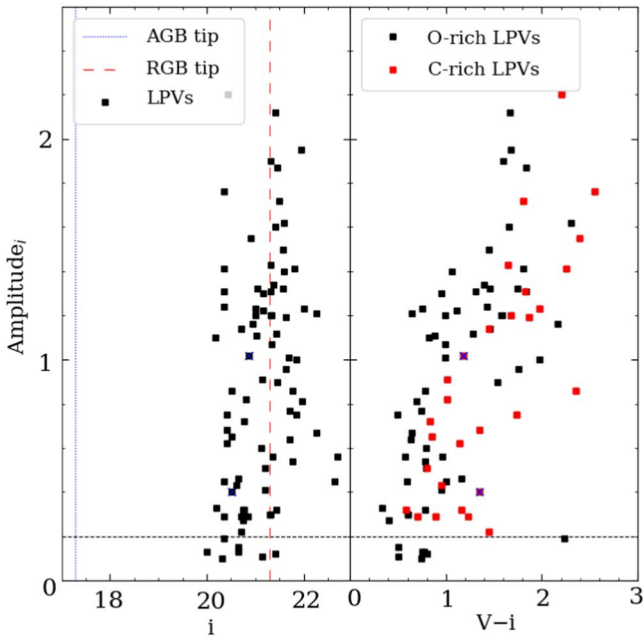


**Figure 9.** Amplitude of variability vs. magnitude in the *i* band (left panel) and vs. color (right panel). Vertical blue and red dashed lines represent the tips of the AGB and RGB, respectively. A 0.2 mag amplitude (horizontal black dashed line) is the threshold for distinguishing LPVs from other candidates.

dashed line (0.2 mag) illustrates the LPV amplitude threshold (Saremi et al. 2020), and the blue dotted and red dashed lines are the tips of the AGB and RGB, respectively (see Section 5). It can be seen that LPV stars with larger amplitudes tend to be redder than those with smaller amplitudes. The right panel of Figure 9 shows the amplitude in the *i* band as a function of ( $V-i$ ) color. The amplitude almost increases with color for more candidates. The stars become redder and fainter as they evolve in the giant star branch. During the evolution of stars along the AGB they become more luminous, so dust must attenuate their light if they appear fainter. Additionally, the amplitude of the variability increases in the AGB phase as they evolve (Wood et al. 1992; McDonald & Zijlstra 2016; McDonald & Trabucchi 2019). The larger amplitude can be explained by the lower luminosity of lower-mass AGB stars; thus, RSGs typically have a lower amplitude (Wood et al. 1992; Wood 1998; Whitelock et al. 2003; van Loon et al. 2008).

The carbon-rich variable candidates of the INT survey, which are classified on the basis of birth mass (see Section 6), are shown in red squares in the right panel of Figure 9. The amplitudes of this sample almost increase with increasing reddening, just as in the Spitzer observations of C-rich variables in the LMC and IC 1631 (Whitelock et al. 2017). Dust-enshrouded variables that have larger amplitudes experience more mass loss and become redder (Whitelock et al. 1991). Further, oxygen-rich variable candidates in the INT survey (black squares in the right panel of Figure 9) with a redder color have a larger amplitude.

A total of seven stars with amplitudes less than 0.2 mag in the *i* band in CCD4 and four within two half-light radii were excluded from the variability analysis. LPVs have variability amplitudes greater than 0.2 mag, and we are unsure of the nature of the variable candidates with amplitudes less than 0.2 mag.

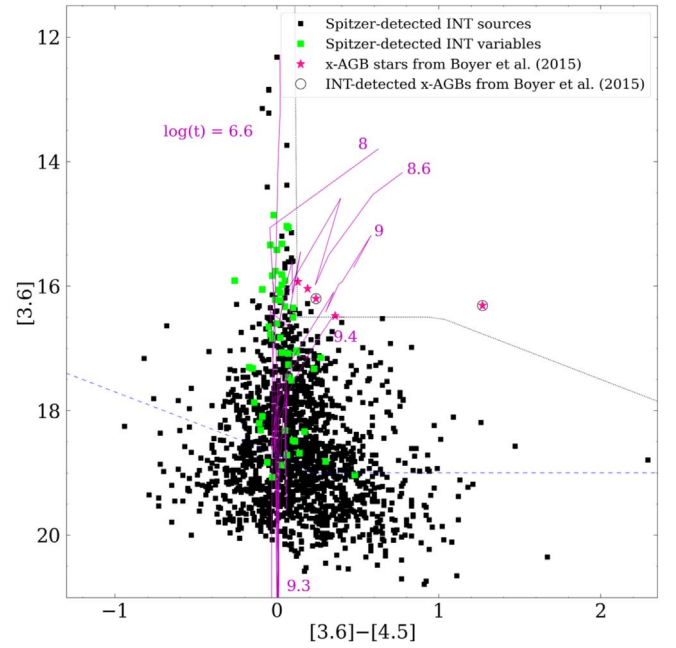


**Figure 10.** CMD of Spitzer-detected INT sources. Spitzer-detected LPVs are highlighted as green squares, and PADOVA isochrones from Marigo et al. (2017) are marked in magenta. The blue dashed line represents the 75% completeness limit of Spitzer data, and the dotted black line separates the plausible region of x-AGB stars (Boyer et al. 2015b).

## 4. Crossmatch with Other Catalogs

### 4.1. Spitzer Catalog Cross-identification

A cross-correlation was carried out between the And IX INT catalog and mid-IR data from the Spitzer Space Telescope, IRAC, in the 3.6 and 4.5  $\mu\text{m}$  bands as part of the DUST in Nearby Galaxies with Spitzer survey (DUSTiNGS; Boyer et al. 2015a). The two catalogs have 1638 common sources within two half-light radii of the center, out of which 50 ( $\sim 3\%$ ) are INT LPV candidates. DUSTiNGS reported five extreme AGB (x-AGB) candidates (Boyer et al. 2015b), with only two detected in our survey (black open circles in Figure 10) as LPV candidates (#5671 and #4433) and two others as part of the nonvariable population (#3770 and #5025). This is as in Boyer et al. (2015b), which detailed that because of imaging artifacts some stars may appear artificially variable in a survey. We estimated a variability index for these two nonvariable stars that is less than the variability threshold in their magnitude range, and also their light curves do not show apparent variability. Our survey did not observe the last example because it is located outside the INT/WFC’s CCD4; therefore, it is unlikely to be part of And IX’s population, as it lies outside the two half-light radii. In Goldman et al. (2019) just one of these LPV candidates was introduced with clear variability. This x-AGB (#5671) is also detected in our survey within the half-light radius of And IX. According to Goldman et al. (2019), this candidate has a period of 467 days and an amplitude of 0.8 mag. There is also a huge difference in color between it and the rest of the x-AGBs, with a color of  $[3.6]-[4.5] = 1.26$  mag, as shown in Figure 10. Two x-AGBs sources detected as LPVs in our survey with sinusoidal fits are presented in Figure 11, along with their mass-loss rate ( $\dot{M}$ ; see Section 7.2) and amplitude in the *i* band (amplitude<sub>*i*</sub>) based on our calculations. In our estimation, LPVs #5671 and #4433

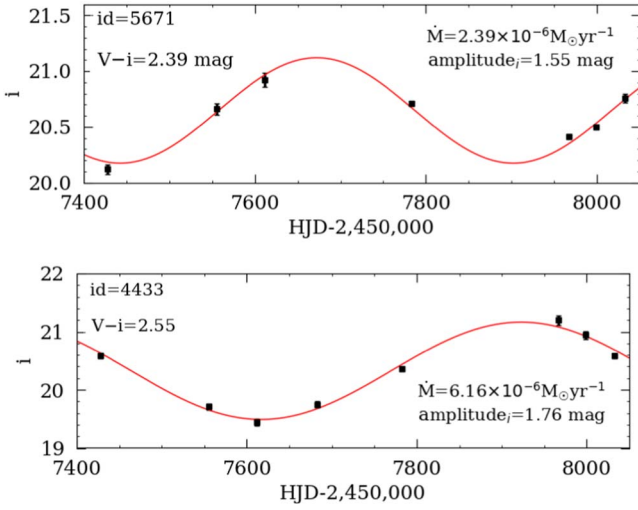


**Figure 11.** Two light curves of mutual x-AGBs in the INT survey and DUSTINGS catalog of variable Spitzer sources (Boyer et al. 2015b) with sinusoidal fits as red curves.

have periods of 530 days (which is very close to Goldman et al.’s 2019 estimate of 467 days) and 585 days, respectively.

#### 4.2. Wide-field Infrared Survey Explorer Catalog Cross-identifications

The WISE All-Sky data release 2013 (Cutri et al. 2021) in the  $W_1 = 3.35$ ,  $W_2 = 4.60$ ,  $W_3 = 11.56$ , and  $W_4 = 22.09 \mu\text{m}$  bands was cross-correlated with the INT catalog of And IX. A total of 864 stellar sources are identified between the INT and the WISE, of which 19 are among the INT survey’s variable candidates. The mutual LPVs between the INT and WISE are low because most of them are in dense regions where we do not get any WISE matches due to the limited angular resolution of WISE. Figure 12 shows a comprehensive CMD of the And IX population with common LPVs in INT, Spitzer, WISE, and SDSS. Matched LPVs between WISE and INT are marked with yellow circles. Figure 13 shows mutual stars from the WISE and INT surveys in four subplots. The Spitzer and SDSS surveys have a better photometric quality than WISE and have more stars in common with the INT survey. According to their SEDs (Figure A1), the  $W_4$  and some  $W_3$  data are too bright compared to the other bands. A poor spatial resolution ( $6''.5$  and  $12''.0$  for  $W_3$  and  $W_4$ , respectively) could have contributed to this.

#### 4.3. Sloan Digital Sky Survey Catalog Cross-identifications

We crossmatched the INT catalog with the SDSS Data Release 12 (Planck Collaboration et al. 2014), the last data released from SDSS-III, in five bands,  $u$ ,  $g$ ,  $r$ ,  $i$ , and  $z$ , from 2008 to 2014. The number of common sources between the SDSS catalog and master catalog of And IX is  $\sim 2680$ , of which 27 are LPVs. More than 80% of the matched sources have magnitude differences less than  $\Delta i < 1$  mag, as we used SDSS photometry to transform our magnitude to the photometric standard system (Landolt). Spitzer data are available for all 27 LPVs that are mutual between the SDSS and INT (pink stars in Figure 12).

In the INT survey, an observation was made on October 21 in the Landolt  $I$  filter. A transformation equation (Jordi et al. 2006) must be used to convert the Landolt  $I$  filter to the Sloan  $i$

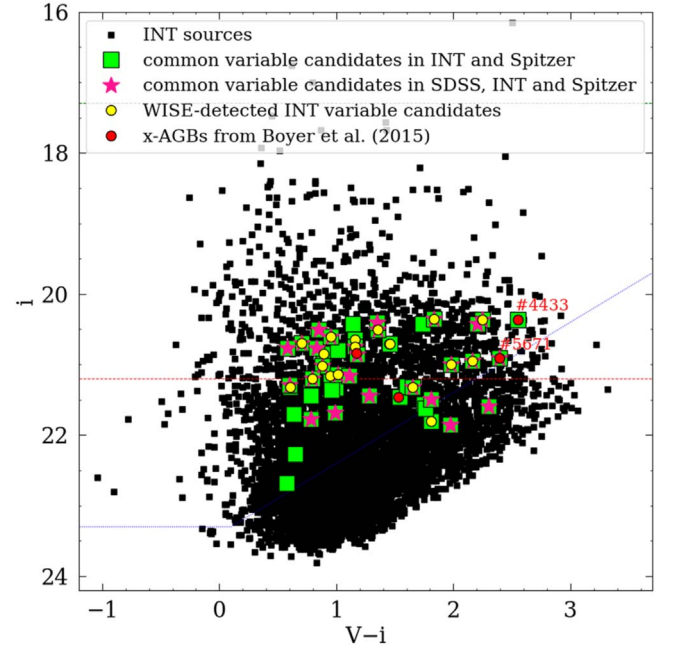


**Figure 12.** CMD of the mutual sources from the INT, Spitzer, WISE, and SDSS surveys within two half-light radii of And IX. Four x-AGBs from Boyer et al. (2015b) are marked with red circles. The AGB tip and RGB tip are illustrated by the green and red dashed lines, respectively. The blue dashed line represents the estimated completeness limit. Candidates #5561 and #4433 are mutual x-AGBs between the INT and Spitzer surveys.

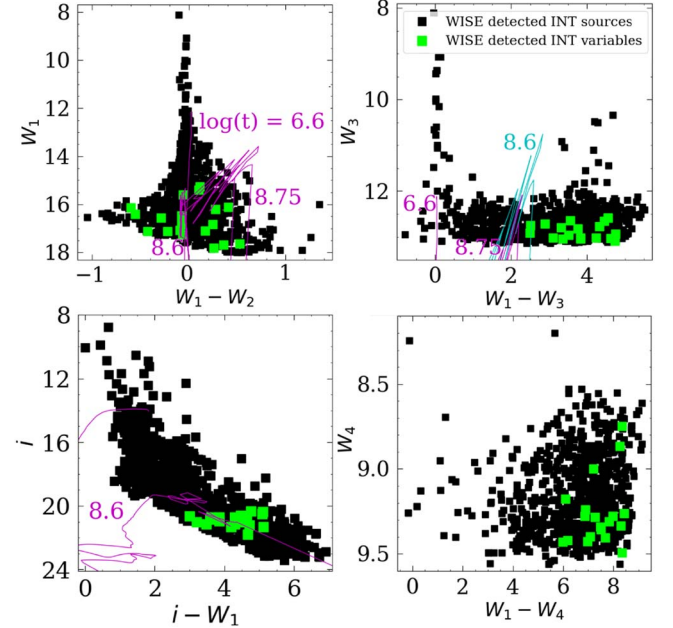


**Figure 13.** CMDs of mutual sources from the INT and WISE surveys. Green squares represent mutual LPVs between INT and WISE. The Padova isochrones (Marigo et al. 2017) are also marked in magenta and blue.

filter for the 230 mutual stars between the SDSS catalog and frame in the Landolt  $I$ , but since we do not have color in the Landolt system we use the color ( $i - z$ ) from the SDSS catalog, which has observation in the Landolt  $I$ . Due to the short exposure time of this frame (Table 3), fewer stars were identified than between the master catalog and the SDSS catalog. Figure 14 shows the magnitude differences in the



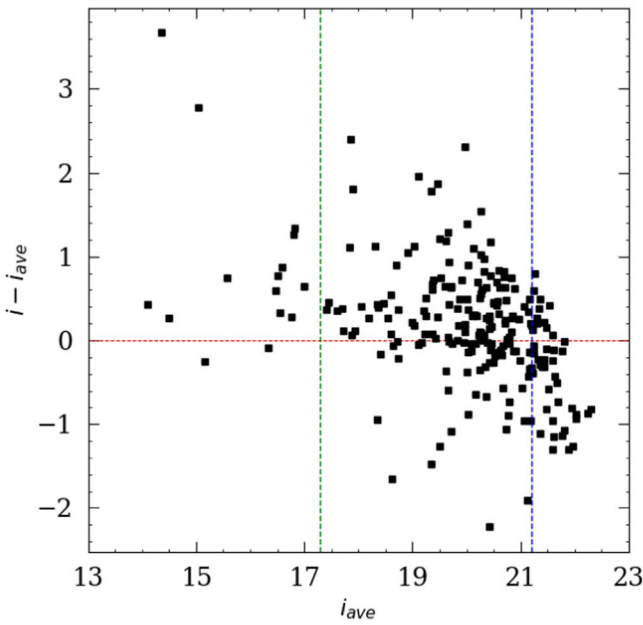


**Figure 14.** The difference of the calculated magnitude in the Sloan  $i$  filter based on the transformation equation (Jordi et al. 2006) with the average magnitude of all frames except October 21 vs. average magnitude for nonvariable stars. The tips of the AGB and RGB are shown with vertical green and blue lines at 17.29 and 21.20 mag, respectively.

Sloan  $i$  filter on October 21 with the average magnitude ( $i_{ave}$ ) in all observation frames (except October 21) for nonvariable stars versus the average magnitude.

There is a large scatter for the magnitude range of interest (between the RGB tip and AGB tip), which makes the filter transformation inaccurate. As a further illustration, in Figure 15 we plot the magnitude differences between the SDSS and INT catalogs ( $i_{INT} - i_{SDSS}$  vs.  $i_{INT}$ ). The magnitude difference between the two surveys is distributed around zero, which indicates the accuracy of magnitude calibration, but the scatter is still quite large. As a result, SDSS colors cannot be used in transformation equations to estimate  $i$ -band magnitudes for LPV identification, which requires high accuracy in the magnitude estimation of any epoch.

### 5. Surveying the Physical Parameters of And IX

We present the And IX stellar density profile (in pink) and surface brightness ( $\text{mag arcsec}^{-2}$ ) (in black) as a function of galactocentric distance in Figure 16. A half-light radius of  $2'.50 \pm 0'.26$  ( $597^{+62}_{-67}$  pc) results from the calculation of the half-area under the most optimal exponential fit (blue curve) to the number density and surface brightness data. Our calculation agrees well with the McConnachie (2012) estimate of about  $2'.5 \pm 0'.1$ . In addition, radii of  $2.5 \pm 0.1$ ,  $2.6 \pm 0.1$ , and  $2'.7 \pm 0'.2$  were estimated for the half-light radius by Collins et al. (2010) considering the best fit of the exponential, Plummer, and King models, respectively, to the distribution of number density as a function of radius.

The magnitude of the tip of the RGB, as a distance indicator, has been used to estimate the distance of the galaxy (Lee et al. 1993). On reaching the end of the RGB, stars ignite helium in their cores. At the tip of the RGB, stars reach maximum luminosity through helium flashes. The TRGB magnitude in the  $I$  band has the least dependence on a star's age and chemistry, making it the most reliable magnitude to use as a

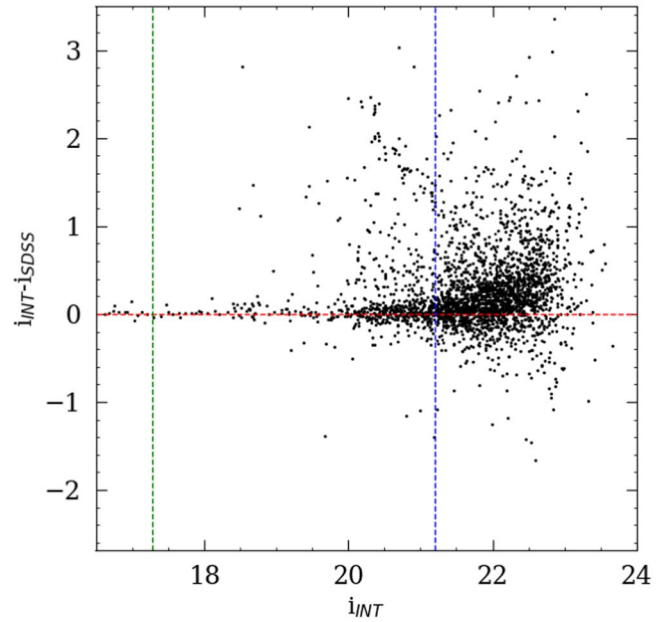


**Figure 15.** Magnitude differences between the INT catalog and SDSS of And IX, plotted against  $i$  magnitude of our catalog. The tips of the AGB and RGB are shown with vertical green and blue lines at 17.29 and 21.20 mag, respectively.

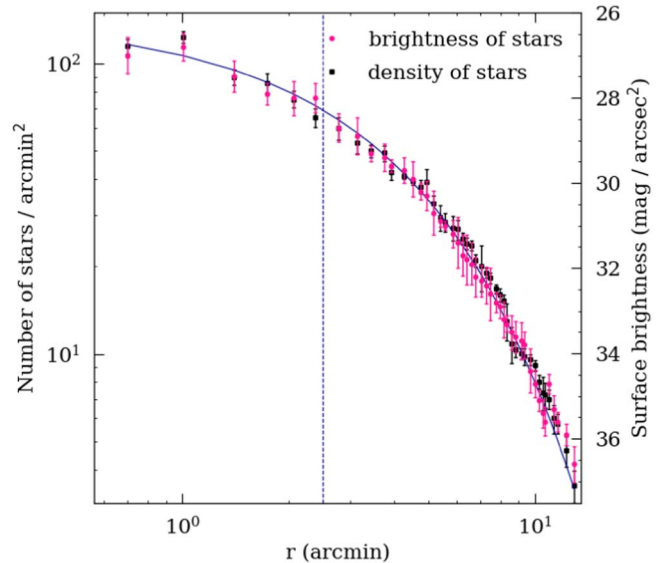


**Figure 16.** The stellar number density and surface brightness of And IX with the best exponential fit to the data (blue curve) as a function of galactocentric distance. The blue dashed line represents the half-light radius ( $2'.50 \pm 0'.26$ ). The vertical error bar results from the Poisson uncertainty of the counts.

standard candle (Lee et al. 1993). It was not possible to convert the photometry bands to the  $I$  band using the transformation equations<sup>12</sup> via the Johnson–Cousins system due to the lack of a third filter. Therefore, we calculated the TRGB magnitude in the  $i$  band.

A population of stellar sources in an area within two half-light radii ( $\sim 0.022 \text{ deg}^2$ ) is selected to estimate the distance of the galaxy, as used in McConnachie et al. (2004). This region is located between two pink lines (left panel in Figure 17) of

<sup>12</sup> <https://www.sdss3.org/dr8/algorithms/sdssUBVRITransform.php>

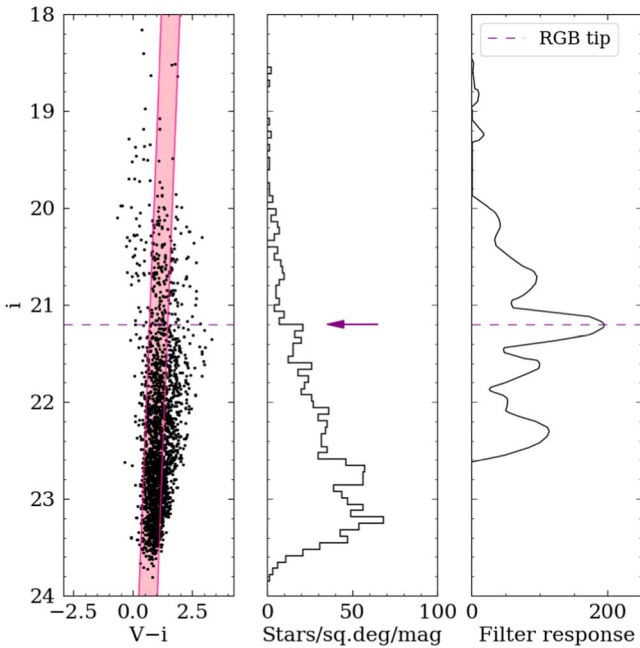


**Figure 17.** The left panel shows the And IX sources within two half-light radii. The middle panel represents a histogram of the luminosity function. The right panel shows the Sobel filter response for the tip of the RGB with edge detection. The tip of the RGB is detected at  $i = 21.20_{-0.15}^{+0.05}$  mag and marked on the CMD by a horizontal purple dotted line and on the luminosity function by an arrow.

$0.28 < V - i < 1.07$  mag and  $18.51 < i < 23.81$  mag to isolate the populations in the red giant branch. The magnitude of the TRGB can be calculated by constructing the  $i$ -band luminosity distribution as a binned histogram with 0.05 mag (middle panel in Figure 17). By convolving the smooth luminosity function with the summation of the normalized Gaussian distribution (Sakai et al. 1996) through a Sobel edge kernel  $[-2, -1, 0, +1, +2]$ , the position of the tip of the RGB at which the convolution is maximum is determined (right panel in Figure 17; Lee et al. 1993).

The distance modulus of  $24.56_{-0.15}^{+0.05}$  mag ( $\sim 816.58_{-54.50}^{+19.02}$  kpc) results from the tip of the RGB at  $i = 21.20_{-0.15}^{+0.05}$  mag (highlighted in purple in Figure 17). In this derivation, a correction of  $2.086 \times E(B - V)$  with 0.075 mag as reddening (Schlegel et al. 1998) is used for the Galactic extinction in the  $i$  band. In addition, we adopt an absolute magnitude of  $-3.52$  mag for the tip of the RGB in the  $i$  band based on the PARSEC isochrones in the SDSS photometry system (Bressan et al. 2012). Estimates of the distance modulus to And IX vary from  $23.89_{-0.08}^{+0.31}$  mag (Weisz et al. 2019a) to  $24.42 \pm 0.39$  mag (Collins et al. 2010).

A CMD of the stellar population of And IX within two half-light radii ( $\sim 5'$ ) is shown in Figure 18. All LPV candidates and those with amplitude  $i < 0.2$  mag are marked in green and orange squares, respectively. The spatial distribution of the variable candidates within two half-light radii is shown in pink circles in Figure 1. The overlaid Padova<sup>13</sup> stellar evolutionary tracks, illustrated in magenta, range from  $\sim 31.62$  Myr to 10 Gyr (Marigo et al. 2017). A distance modulus of  $24.56_{-0.15}^{+0.05}$  mag and a metallicity  $Z = 0.0001$  are used for all stellar tracks in this paper. A total of 8653 stellar sources and 84 variable

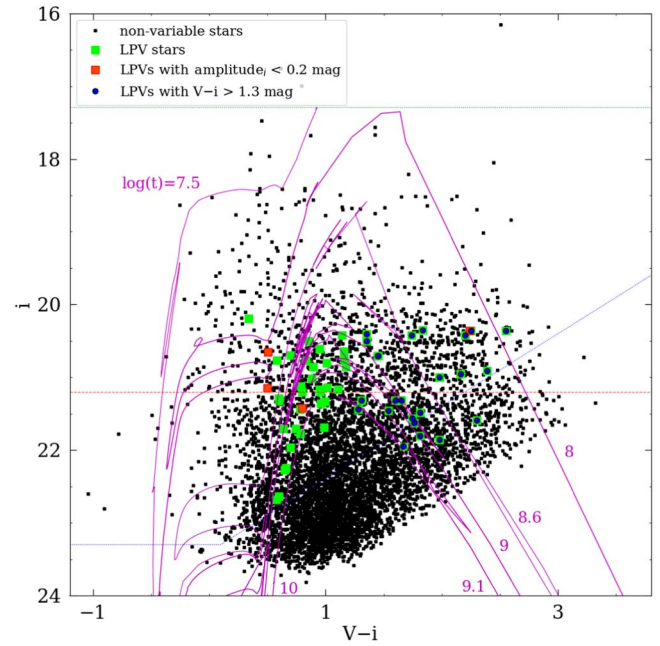


**Figure 18.** CMD of And IX sources in an area within two half-light radii. The variable candidates are marked with green squares and those with amplitude  $i < 0.2$  mag with orange squares. The completeness limits of the photometry (blue), the AGB tip (green), and the RGB tip (red) are shown in the graph. The Padova isochrones (Marigo et al. 2017) are also marked in magenta. Dust correction will be applied to the LPVs shown in blue.

candidates were detected in an area of  $11.26 \times 22.55$  arcmin<sup>2</sup> ( $2.69 \times 5.39$  kpc<sup>2</sup>), which corresponds to CCD4 of the WFC.

AGB stars at the tip of the AGB are optically obscured by dust due to high mass loss. The Chandrasekhar core mass for the classical AGB limit is obtained as  $M_{\text{bol}} = -7.1$  mag ( $M_{\text{bol}} < -8$  mag for supergiants) considering the classical core mass–luminosity relation (Zijlstra et al. 1996). From the Padova evolutionary model, the classical AGB limit is estimated to be  $\log(t) = 7.5$  ( $t = 31.62$  Myr) for the tip of the AGB (green dashed line) with  $i = 17.29$  mag. Figure 18 also shows a red dashed line representing the tip of the RGB at  $i = 21.20$  mag and the completeness limit of the photometry in blue.

## 6. From Variable Candidates to Star Formation History

As mentioned, to reconstruct the SFH of And IX we will use the LPV candidates, since there is a relation between their luminosity and their birth mass. This is possible by Padova stellar evolutionary tracks, which link the luminosity of LPVs to their birth mass. The Padova tracks are a comprehensive description of stellar evolution from the first thermal pulse of the AGBs to the post-AGB phase. The effects of circumstellar extinction and different chemical compositions of dust are also considered (Marigo et al. 2017). The age and pulsation duration of LPVs are derived from the birth mass–age and birth mass–pulsation duration relationships. Suitable coefficients for these relations with a distance modulus of  $24.56_{-0.15}^{+0.05}$  mag and metallicities of  $Z = 0.0001$ ,  $Z = 0.0002$ , and  $Z = 0.0003$  were derived by Saremi et al. (2021).

As AGB stars evolve, their bolometric luminosity should increase; but as they become cooler and more dust-enshrouded, their optical brightness will decrease. In other words, AGB stars reemit the absorbed IR radiation at larger wavelengths.

<sup>13</sup> <http://stev.oapd.inaf.it>

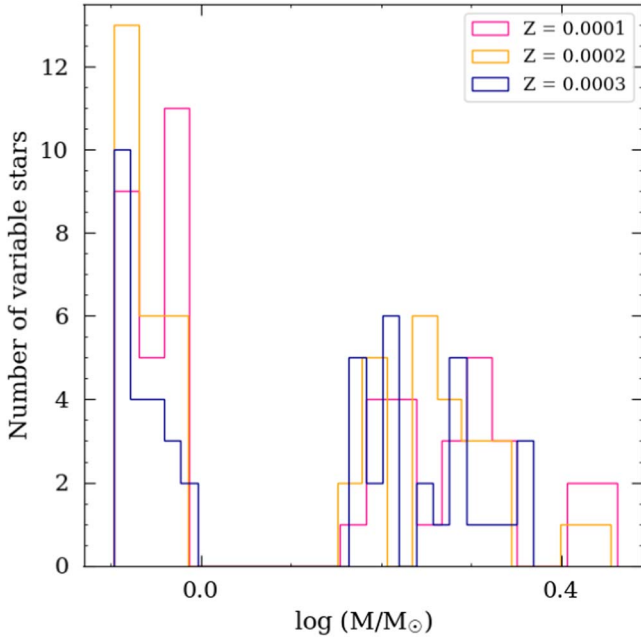


**Figure 19.** Histogram of the number of variable stars within two half-light radii with metallicities  $Z = 0.0001$  (pink),  $Z = 0.0002$  (orange), and  $Z = 0.0003$  (blue).

The AGB stars become fainter and redder due to extinction, both from interstellar dust and circumstellar dust. It is therefore necessary to apply a magnitude correction to stars enveloped by dust in addition to the Galactic-extinction correction.

We apply a magnitude correction for the LPVs with  $V-i > 1.3$  mag to bring them back to  $V-i = 1$  mag. The slopes of the isochrones for O-rich evolutionary tracks tend to redden faster compared to C-rich tracks. In our sample, the O-rich and C-rich stars have average slopes of 3.31 and 2.37 mag mag<sup>-1</sup>, respectively. The calculations were performed using the isochrones from Figure 18. Blue points in Figure 18 indicate LPV candidates affected by circumstellar dust, so the magnitude correction will be applied. The correction equation with  $a$  as the slope of the isochrones is as follows:

$$i_0 = i + a[(V - i)_0 - (V - i)]. \quad (3)$$

First, a carbon-correction equation is applied to our sample by assuming that our LPVs are C-rich. The birth mass is derived using the corrected magnitude in the  $i$  band and the relation between birth mass and luminosity. This assumption is correct if  $1.5 \leq M/M_\odot \leq 4$  (Saremi et al. 2021). Otherwise, our sample should be dereddened by the oxygen-correction equation (see Section 7 for more details on the mass range). The histogram in Figure 19 shows the number of variable stars in different mass ranges for three metallicities. There are no variable stars with a mass of 1–1.5  $M_\odot$  in this galaxy, according to the histogram.

### 6.1. Calculation Method for Star Formation Rate

Based on the mass, age, and pulsation duration of the LPVs, the star formation rate (SFR) is calculated. We use the mass–luminosity relation to convert the  $i$ -band magnitudes of the LPV stars to their masses. There is a correlation between the most luminous point in each isochrone and its associated mass. Using a function fitted to all points derived from different isochrones, constant coefficients can be obtained for different

luminosity intervals at different magnitude intervals to calculate the birth mass. Here, we used the coefficients of the best fit of the function reported by Saremi et al. (2021) to derive the relationships between mass and luminosity, mass and age, and mass and pulsation duration.

The SFR,  $\xi(t)$  ( $M_\odot \text{ yr}^{-1}$ ), as a function of time is used to derive the SFH. The method used in this paper was adapted from Javadi et al. (2011b), Hamedani Golshan et al. (2017), and Javadi et al. (2017), and has also been used to reconstruct the SFHs of other dwarf galaxies in the Local Group by Rezaeikh et al. (2014), Hamedani Golshan et al. (2017), Hashemi et al. (2019), Navabi et al. (2021), Saremi et al. (2021), and Parto et al. (2023). In this method, the SFR is derived based on a Kroupa (2001) initial mass function (IMF) to describe the initial mass distribution of stars rather than the number of stars. The SFR is calculated by considering the LPV mass in a range from  $m(t)$  to  $m(t + dt)$ , where  $\delta t$  is the pulsation duration (the total amount of time a star spends as an LPV), and  $dn'$  is the number of stars in each period. The SFR is given by

$$\xi(t) = \frac{dn'(t)}{\delta t} \frac{\int_{m(t)}^{m(t+dt)} f_{\text{IMF}}(m) m dm}{\int_{m(t)}^{m(t+dt)} f_{\text{IMF}}(m) dm}. \quad (4)$$

Massive stars evolve more quickly, and their pulsation phases last only a short time. However, low-mass stars spend more time in this phase and are more likely to appear in the pulsation phase. Thus, we use pulsation duration in this formula as a correction factor. By considering a Poisson statistic distribution of the number of stars in each bin as  $N$ , the statistical error is calculated as

$$\sigma = \frac{\sqrt{N}}{N} \xi(t). \quad (5)$$

### 6.2. The Star Formation History in And IX

The birth mass, age, and pulsation duration are calculated from the brightness of LPVs. Stars are sorted by mass and classified into bins with the same number of stars, so the mass span in each interval is specified for IMF integration.

Metallicity is an important factor in stellar evolutionary tracks, so it can affect the determined SFH, as well. According to estimates, And IX’s metallicity is  $[\text{Fe}/\text{H}] = -2.2 \pm 0.2$  dex ( $\sim Z = 0.0001$ ) in Collins et al. (2010) and McConnachie (2012); Wojno et al. (2020) further calculated the metallicity to be  $[\text{Fe}/\text{H}] = -2.03 \pm 0.01$  dex ( $\sim Z = 0.0002$ ). Kirby et al. (2013) reported a mean metallicity  $[\text{Fe}/\text{H}] = -1.93 \pm 0.20$  dex ( $\sim Z = 0.0002$ ), assuming a solar abundance of  $12 + \log(\text{Fe}/\text{H}) = 7.52$ . The metallicity of a galaxy varies during its evolution, so in this study we consider metallicity  $Z = 0.0002$  as well as a more metal-rich estimate  $Z = 0.0003$  in addition to the main metallicity  $Z = 0.0001$ .

Figure 20 illustrates the SFHs in two half-light radii corresponding to metallicities  $Z = 0.0001$ ,  $Z = 0.0002$ , and  $Z = 0.0003$ . Each age bin length and the statistical error on the SFR are represented by horizontal and vertical error bars, respectively. In this paper, we use the  $\Lambda$ CDM standard model with cosmological parameters, the Hubble constant  $H_0 = 67.3 \pm 1.2 \text{ km s}^{-1} \text{ Mpc}^{-1}$ , the matter density parameter  $\Omega_m = 0.315 \pm 0.017$ , and the physical densities of baryons and cold dark matter  $\Omega_b h^2 = 0.02205 \pm 0.00028$  and  $\Omega_c h^2 = 0.1199 \pm 0.0027$ , respectively, to calculate the redshift (Planck Collaboration et al. 2014).

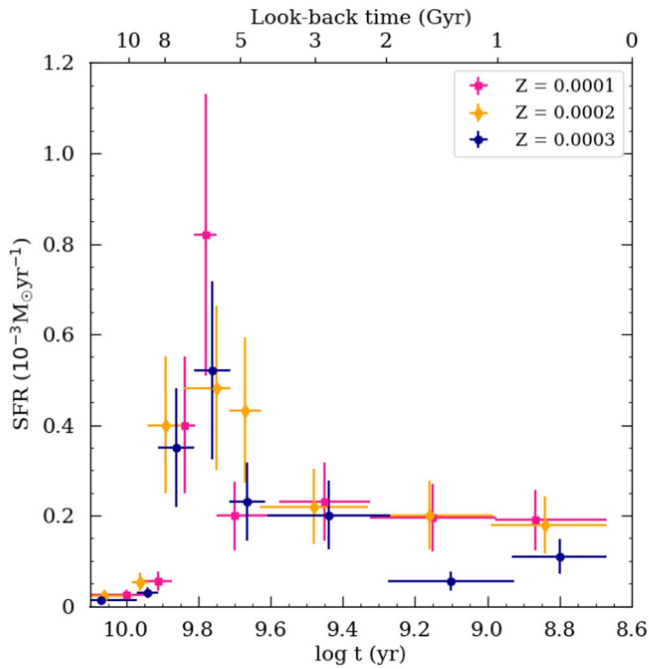


**Figure 20.** SFHs of And IX for metallicities of  $Z = 0.0001$  (pink),  $Z = 0.0002$  (orange), and  $Z = 0.0003$  (blue) within two half-light radii ( $\sim 0.022 \text{ deg}^2$ ).

The star formation epochs occurred between 500 Myr ( $\log t = 8.67$ ) and 13 Gyr ago ( $\log t = 10.1$ ). Assuming  $Z = 0.0001$ , the SFR reached a maximum of  $8.2 \pm 3.1 \times 10^{-4} M_{\odot} \text{ yr}^{-1}$  around 6 Gyr ago. During this period, the SFR peaked at  $4.8 \pm 1.8 \times 10^{-4} M_{\odot} \text{ yr}^{-1}$  and  $5.2 \pm 2.0 \times 10^{-4} M_{\odot} \text{ yr}^{-1}$  for metallicities  $Z = 0.0002$  and  $Z = 0.0003$ , respectively.

Comparing the SFR at different metallicities shows that  $Z = 0.0001$  produces the highest peak of SFR due to its more metal-poor environment. Generally, the SFR decreases with increasing metallicity except for at 1.41, 5.01, and 6.02 Gyr ago. SFR distributions for metallicities of  $Z = 0.0001$  and  $Z = 0.0003$  are used for this comparison. Unlike the two other metallicities, the SFR at  $Z = 0.0003$  peaks at 630 Myr ago (corresponding to errors, 850–457 Myr ago) with a rate of  $11.0 \pm 4.0 \times 10^{-5} M_{\odot} \text{ yr}^{-1}$ .

Cross-correlation using the Boyer et al. (2015b) catalog of x-AGB stars provided the detection of two x-AGBs. Based on Boyer et al.’s (2015a) classification scheme, x-AGB stars are variables with  $M_{3,6} < 8 \text{ mag}$  and colors  $[3.6] - [4.5] > 0.1 \text{ mag}$ . They produce more than 75% of the dust produced by cool evolved stars, but they represent less than 6% of the total population of AGBs (Boyer et al. 2012). Two stars with masses exceeding  $1.5 M_{\odot}$  and an estimated 1 Gyr to 1.58 Gyr of age have been identified as carbon stars. As a result of the existence of these C-rich AGB stars, there is a possibility that other C-rich AGBs are responsible for the revival of the SFH. Also, these two carbon stars may be older AGBs that are going through the bright part of their thermal-pulse cycle. However, more research is necessary to determine if dusty LPV mass loss has recently increased the SFR.

The total stellar mass over a specified time is calculated by aggregating  $\xi(t)$  over that period. A total stellar mass of  $3.0 \times 10^5 M_{\odot}$  is obtained for a metallicity of  $Z = 0.0001$  within two half-light radii. In And IX, the stellar mass is reduced by 20% ( $\sim 2.4 \times 10^5 M_{\odot}$ ) and 23% ( $\sim 2.3 \times 10^5 M_{\odot}$ ) at

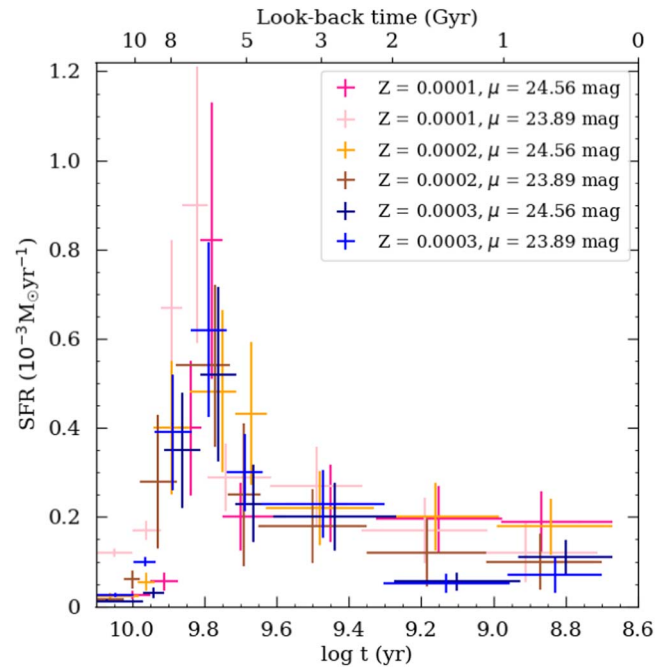


**Figure 21.** SFHs of And IX for three metallicities of  $Z = 0.0001$ ,  $Z = 0.0002$ , and  $Z = 0.0003$  within two half-light radii ( $\sim 0.022 \text{ deg}^2$ ) with a distance modulus of  $23.89_{-0.08}^{+0.31} \text{ mag}$  (Weisz et al. 2019a) and  $24.56_{-0.15}^{+0.05} \text{ mag}$ .

metallicities of  $Z = 0.0002$  and  $Z = 0.0003$ , respectively. This study observed a decrease in total stellar mass due to increasing metallicity. Considering a metallicity of  $[\text{Fe}/\text{H}] = -2.03 \pm 0.01$  ( $\sim Z = 0.0002$ ), Wojno et al. (2020) estimated a stellar mass of  $\sim 2.4 \times 10^5 M_{\odot}$  ( $\log(M/M_{\odot}) = 5.38 \pm 0.44$ ). According to the aforementioned papers, the estimated stellar mass is similar.

While changing the distance modulus and Galactic extinction do not affect the age–mass and pulsation duration–mass relations, it will change the magnitudes of the LPV stars and hence their mass and the SFH of the galaxy. Figures 21 and 22 are plotted separately in order to illustrate the potential differences between the effects of the distance modulus and Galactic extinction on SFR. A comparison of the SFHs of And IX for the distance modulus derived in this paper ( $24.56_{-0.15}^{+0.05} \text{ mag}$ ) and the lowest distance modulus reported ( $23.89_{-0.08}^{+0.31} \text{ mag}$ ; Weisz et al. 2019a) is shown in Figure 21. As can be seen, the SFHs exhibit similar behavior, and there is only a shift toward recent times with increasing distance modulus. The Galactic extinctions for And IX are estimated as  $A_i = 0.127 \text{ mag}$  ( $E(B-V) = 0.075$ ; McConnachie 2012) and  $A_i = 0.129 \text{ mag}$  ( $E(B-V) = 0.076$ ; Conn et al. 2012) from Schlafly & Finkbeiner (2011). In Figure 22, we compare the SFH of the galaxy assuming an average of the reported Galactic extinctions ( $A_i = 0.128 \text{ mag}$ ) with the SFH of And IX that does not account for Galactic extinction ( $A_i = 0 \text{ mag}$ ). There is no significant difference in the results, but the SFH is shifted to earlier epochs when Galactic extinction is ignored.

We estimate the total stellar mass of And IX in the lowest distance modulus ( $23.89_{-0.08}^{+0.31} \text{ mag}$ ; Weisz et al. 2019a)  $\sim 3.50 \pm 0.50 \times 10^5 M_{\odot}$  with  $A_i = 0.128 \text{ mag}$ , and  $\sim 3.10 \pm 0.30 \times 10^5 M_{\odot}$  with  $A_i = 0 \text{ mag}$ , at  $Z = 0.0001$ . At a metallicity of  $Z = 0.0002$ , the total stellar mass is  $\sim 2.70 \pm 0.40 \times 10^5 M_{\odot}$  with  $A_i = 0.128 \text{ mag}$  and  $\sim 2.60 \pm 0.10 \times 10^5 M_{\odot}$  with  $A_i = 0$ . The total stellar mass of And IX at  $Z = 0.0003$  is  $\sim 2.50 \pm 0.40 \times 10^5$

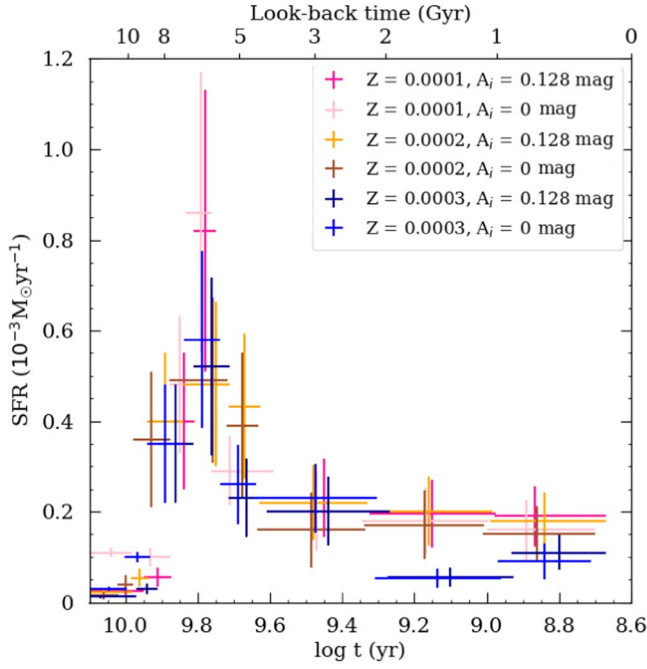


**Figure 22.** SFHs of And IX for three metallicities of  $Z = 0.0001$ ,  $Z = 0.0002$ , and  $Z = 0.0003$  within two half-light radii ( $\sim 0.022 \text{ deg}^2$ ), applying the Galactic extinction in filter  $i$  ( $A_i = 0.128 \text{ mag}$ ) and without considering the extinction ( $A_i = 0 \text{ mag}$ ).

$M_\odot$  and  $\sim 2.46 \pm 0.20 \times 10^5 M_\odot$  considering  $A_i = 0.128 \text{ mag}$  and  $A_i = 0 \text{ mag}$ , respectively.

As a function of look-back time and redshift, Figure 23 shows the cumulative star formation (colors based on Figure 20). The best exponential fit for our star formation model was obtained with a so-called  $\tau$ -model with  $\tau = 5$ . The following equation describes this SFH with a declining e-folding time,  $\tau$ , which is initiated at  $t_i$  with amplitude  $A$  (Simha et al. 2014):

$$\text{SFR}(t) \propto A e^{-(t-t_i)/\tau}. \quad (6)$$

According to Figure 23, the horizontal dashed line labeled  $90\% M_{\text{tot}}$  indicates the time it took to assemble 90% of the stellar mass (known as the quenching time). In addition, Figure 23 shows the epoch by which 50% of the stellar mass had been formed with a horizontal dashed line, indicating  $50\% M_{\text{tot}}$ . Table 4 summarizes the aggregation time for half ( $t_{50}$ ) and 90% ( $t_{90}$ ) of the total stellar mass at different metallicities of And IX. The first line in  $t_{50}$  and  $t_{90}$  of Table 4 is based on the SFHs in Figure 20 and a distance modulus of  $24.56^{+0.05}_{-0.15}$ , the second line is based on the SFHs with a distance modulus of  $23.89^{+0.31}_{-0.08} \text{ mag}$  in Figure 21. According to Table 4, the aggregation time for 50% and 90% of the total stellar mass move to more recent times in the three metallicities by increasing the distance modulus. Additionally, increasing metallicity has a similar effect on  $t_{50}$  and  $t_{90}$  at the same distance modulus. Our results are consistent with Weisz et al. (2019b), who estimated the quenching time as  $5.1^{+1.8}_{-2.0} \text{ Gyr}$  ago and the aggregation of half of the total stellar mass as  $7.2^{+2.5}_{-0.3} \text{ Gyr}$  ago.

### 6.3. Radial Star Formation History

SFHs in different radial regions within a galaxy may reveal important information regarding the galaxy's formation history.

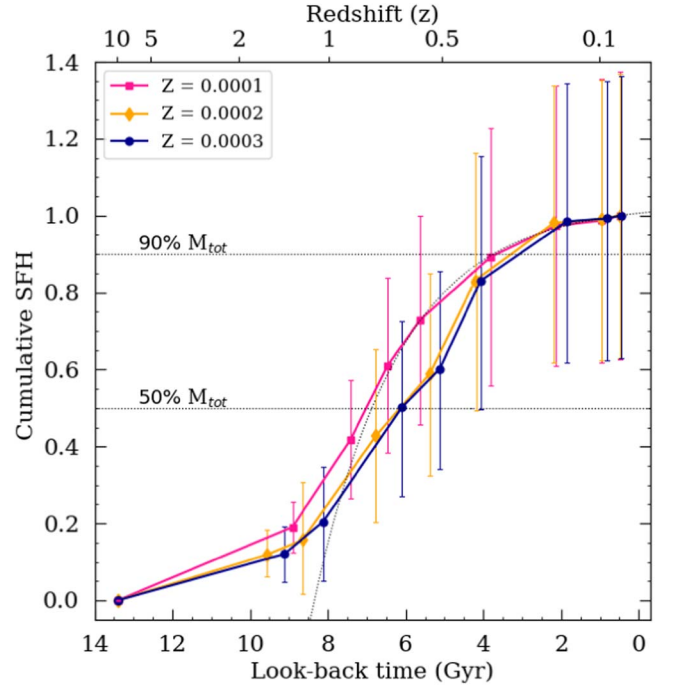


**Figure 23.** Cumulative SFH as a function of look-back time and redshift within two half-light radii of And IX for three different adopted metallicities. Each bin is accompanied by a vertical error bar showing the statistical error of the SFR. The pink curve is also fitted by a  $\tau$ -model exponential function (dotted black curve). Statistical errors in SFRs indicate the cumulative SFH errors for metallicities of  $Z = 0.0001$  (pink error bars),  $Z = 0.0002$  (orange error bars), and  $Z = 0.0003$  (blue error bars).

**Table 4**

Time to Aggregation for Half of the Total Stellar Mass ( $t_{50}$ ) and 90% of the Total Stellar Mass ( $t_{90}$ ) at Different Metallicities

	$\mu$ (mag)	$Z = 0.0001$	$Z = 0.0002$	$Z = 0.0003$
$t_{50}$ (Gyr)	$24.56^{+0.05}_{-0.15}$ <sup>a</sup>	$7.02^{+0.39}_{-0.56}$	$6.15^{+0.77}_{-1.02}$	$6.10^{+0.36}_{-0.97}$
	$23.89^{+0.31}_{-0.08}$ <sup>b</sup>	$8.00^{+0.10}_{-1.30}$	$7.20^{+0.80}_{-0.70}$	$7.10^{+0.30}_{-1.40}$
$t_{90}$ (Gyr)	$24.56^{+0.05}_{-0.15}$	$3.65^{+0.13}_{-1.52}$	$3.29^{+0.97}_{-1.16}$	$3.07^{+1.00}_{-1.39}$
	$23.89^{+0.31}_{-0.08}$	$3.95^{+2.00}_{-0.50}$	$3.40^{+0.40}_{-0.60}$	$3.10^{+0.30}_{-0.40}$

#### Notes.

<sup>a</sup> Estimates based on the distance modulus calculated in this paper.

<sup>b</sup> Estimates based on the distance modulus calculated in Weisz et al. (2019a).

For this, we divided the area of And IX into different radius bins with an equal number of stars to derive the radial gradient of SFH. In Figure 24, the density of the SFR is plotted as a function of logarithmic time in four circular regions for a metallicity of  $Z = 0.0001$ . Due to the four annuli that make up And IX, each region may have a different population of stars. The ratio of the SFR for  $t > 3.16 \text{ Gyr}$  ago ( $\log(t) > 9.5$ ) to that for  $t < 3.16 \text{ Gyr}$  ago ( $\log(t) < 9.5$ ) in the innermost region is  $0.990^{+0.005}_{-0.010}$ , while in the second region ( $\sim 0.35\text{--}0.61 \text{ kpc}$ ) it is  $1.82^{+0.07}_{-0.04}$ . The fraction reaches  $1.45^{+0.03}_{-0.06}$  in the third region and  $3.48^{+0.91}_{-0.40}$  in the outermost region. When moving toward the central regions this ratio decreases, suggesting that younger populations tend to be concentrated there. As a result, star formation began in the outer part and gradually spread inward. In these regions, 20% of the total mass per unit area is formed at the outermost radius, 23% at the middle regions, and the rest

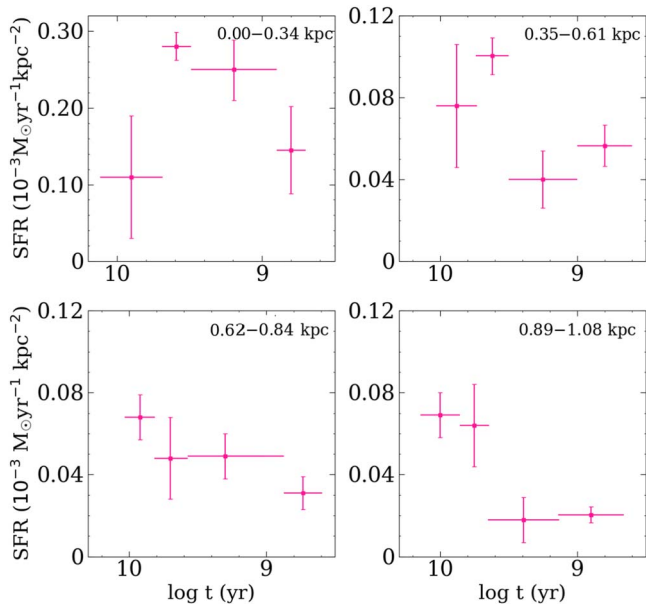


**Figure 24.** SFRs of And IX per unit area within four regions at galactocentric radii for a constant metallicity of  $Z = 0.0001$ .

at the innermost radius. Therefore, the total stellar mass per unit area is more concentrated in the innermost region.

In Figure 25, we divide our sample into two regions ( $r < 0.5$  and  $r > 0.5$  kpc) to examine the radial gradient of SFH for metallicities of  $Z = 0.0001$  (in pink) and  $Z = 0.0003$  (in blue). The star formation pattern suggests the highest SFRs in central regions at later times, which is the opposite of the outer regions. In support of this, the fractions of  $0.720^{+0.003}_{-0.002}$  in  $r < 0.5$  and  $2.13^{+0.77}_{-0.29}$  in  $r > 0.5$  are obtained by estimating the ratio of the older population at  $Z = 0.0001$  compared to the younger population at  $Z = 0.0003$ . When  $r > 0.5$  kpc (estimated ratio greater than unity), older populations form earlier than when  $r < 0.5$  kpc (estimated ratio less than unity). Clearly, this supports an outside-in formation scenario for And IX based on the different age gradients of the populations in the inner and outer parts of the galaxy (Hidalgo et al. 2008, 2013; Benítez-Llambay et al. 2016). The dynamical effect could be another scenario for the distribution of stars in And IX, where stars migrate outwards after forming in more central regions. This is not unexpected, as star formation only occurs if gas cools and falls deeply into the gravitational potential well of a small halo such as And IX; this is a highly nonequilibrium state, and the internal dynamics would gradually cause the stars to fill the gravitational potential well (i.e., migrate outward); tidal stress would exacerbate this.

#### 6.4. Quenching Mechanisms in And IX

Several mechanisms lead to the quenching of a dwarf galaxy. Depletion of cold gas in the reionization era is supposed to affect the shutting down of star formation in UFDs ( $M_V > -6$  mag) and low-mass galaxies ( $M < 10^5 M_\odot$ ; Gnedin 2014; Xu et al. 2016; Wheeler et al. 2019; Applebaum et al. 2021). At  $z = 10$ , low-mass galaxies are expected to be quenched by cosmic reionization, while for more massive galaxies environmental processes have a more significant effect on the cessation of star formation at  $z = 6$  (Wetzel et al. 2015). It can be ruled out with greater certainty that the Epoch of Reionization will not affect And IX’s quiescence since the SFRs are shut down

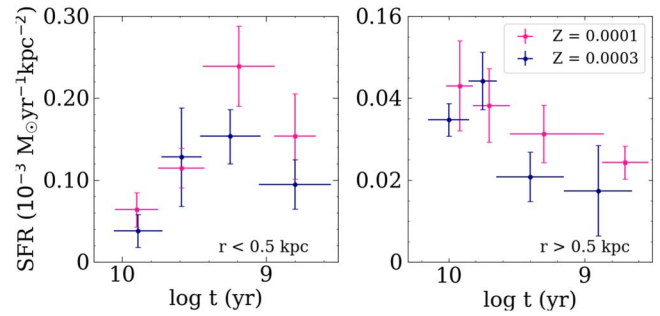


**Figure 25.** SFRs of And IX per unit area with equal numbers of LPV candidates within two regions at galactocentric radii for metallicities of  $Z = 0.0001$  (pink) and  $Z = 0.0003$  (blue).

by  $z = 6$ . Environmental effects, such as ram pressure stripping, tidal effects, and dwarf-galaxy interactions, may quench dwarfs with stellar masses  $10^5$ – $10^7 M_\odot$ . In particular, ram pressure stripping is a noticeable mechanism that stops star formation in galaxies with  $M < 10^7 M_\odot$  (Simpson et al. 2018).

Another factor in the shutting down of star formation of a satellite can be a fall in the virial radius of its host galaxy. For Milky Way dwarf satellite galaxies, the infall time can be calculated using positions, line-of-sight velocities, and proper motions (if measured; Rocha et al. 2012). Since these data are not available for the satellites of Andromeda, cosmological simulation is used to estimate the infall time. In a study by Wetzel et al. (2015), all Milky Way and Andromeda satellites with  $M < 10^8 M_\odot$  were quenched after falling into their host galaxy’s virial radius of less than 2 Gyr, and quenching is more rapid at lower stellar masses. This study estimated infall time using  $N$ -body simulations. Furthermore, D’Souza & Bell (2021) proposed a correlation between quenching time and the time when satellites enter the virial halo of their hosts (accretion time). In M31, massive accretion occurred around 5.5 Gyr ago, around the time most M31 satellites quenched, and also according to our estimate. Using 20 satellites of M31, Weisz et al. (2019b) determined a look-back time of 3–6 Gyr for the assembly of 90% of stellar mass and 6–9 Gyr for the assembly of 50% of stellar mass. Our study also confirms these results. For metallicities of  $Z = 0.0004$  and  $Z = 0.0007$ , Saremi et al. (2021) estimated the quenching time of And I to be about 4 Gyr ago. Similarly, And VII, another satellite of M31, was quenched 5 Gyr ago at  $Z = 0.0007$  and 5.7 Gyr ago at  $Z = 0.0004$  (Navabi et al. 2021). This is also consistent with the quenching time reported in Weisz et al. (2019b).

Environmental processes play an essential role in quenching And IX, a satellite with a stellar mass of  $M \leq 10^8 M_\odot$ . These processes include tidal effects and the depletion of cold gas through M31 (due to proximity). Internal processes also quench star formation, such as galactic winds, supernovae, and stellar feedback, specifically in low-mass dwarfs (Ledinauskas & Zubovas 2020).

## 7. Probing of Dust in And IX

### 7.1. Carbon-rich and Oxygen-rich Circumstellar Envelopes

The carbon abundance in the atmosphere of AGB stars increases after the third dredge-up process, despite the abundance of oxygen before it. Based on carbon and oxygen abundances in the atmosphere, AGBs are generally classified as carbon-rich ( $C/O > 1$ ) or oxygen-rich ( $C/O < 1$ ) (Ren et al. 2022). As metal-poor environments have less oxygen, carbon

stars form more easily since less carbon must be dredged up to achieve  $C/O > 1$  (Leisenring et al. 2008; Ren et al. 2022). AGB star models estimate different thresholds for the third dredge-up, some of which are summarized below. In Magellanic Clouds (MCs), the mass range for C-rich stars is between  $1.3$  and  $4 M_{\odot}$  (van Loon et al. 2005b); Girardi & Marigo (2007) estimate the mass ranges of C- and M-type stars using  $1.5$ – $2.8 M_{\odot}$  for C-rich stars in MC clusters. According to McDonald et al. (2012), the condition of  $C/O > 1$  was first achieved in stars around  $1 M_{\odot}$  in the Sgr dSph galaxy with a metallicity  $Z \sim 4 \times 10^{-3}$ . In the LMC, Goldman et al.'s (2017) estimations of  $M \leq 1.5 M_{\odot}$  and  $M \geq 4 M_{\odot}$  for O-rich stars are based on 1612 MHz circumstellar OH maser emissions from AGB stars and RSGs.

Given the low oxygen abundance in And IX, a range of  $1.5$ – $4 M_{\odot}$  is adopted for the carbon stars (Saremi et al. 2021). In our survey, no LPVs were found in the mass range of  $1$ – $1.5 M_{\odot}$ ; thus, substantial differences are not seen in the number of C- and O-rich LPVs based on these assumptions. As a result, the SFRs are almost the same regardless of the precise choice of the lower end of the C-rich star mass range. The chemical type of stars is determined by their masses, as described in Section 6.

## 7.2. Spectral Energy Distribution Modeling through DUSTY

In this paper, we modeled the SEDs of variables through the DUSTY code, which was written by Ivezić & Elitzur (1997). Modeling the SED requires input data such as stellar temperature, external radiation characteristics, dust properties (e.g., temperature, chemical compositions, grain size distribution), optical depth, and envelope density distribution. We put the star's and dust's temperatures at the inner edge of the circumstellar envelope at  $3000$ – $3500$  K and  $500$ – $1200$  K, respectively (Gail & Sedlmayr 1999; Höfner & Olofsson 2018). The C-rich type is made through the mixture of 85% amorphous carbon (Hanner 1988) and 15% silicon carbide (Pégourié 1988), while the O-rich type is made through the use of astronomical silicates (Draine & Lee 1984). In solving hydrodynamic equations for AGB stars, DUSTY assumes radiatively driven wind. When solving the equations, default parameters (gas-to-dust mass ratio  $\psi_{\odot} = 200$ ,  $L = 10^4 L_{\odot}$ , and  $\rho_{\text{dust}} = 3 \text{ g cm}^{-3}$ ) are adopted. In this case,  $\psi$  is scaled by the relation  $\psi = \psi_{\odot} 10^{-[\text{Fe}/\text{H}]}$ , assuming a reverse metallicity relation with the gas-to-dust mass ratio (van Loon et al. 2005b). Based on trial and error, the optical depth is estimated by comparing the simulated SED to the observed SED. As a result of the scaling relations, the mass-loss rates of LPVs are determined using the following equation (Nenkova et al. 1999):

$$\dot{M} = \dot{M}_{\text{DUSTY}} \left( \frac{L}{10^4} \right)^{3/4} \left( \frac{\psi}{\psi_{\odot}} \right)^{1/2}. \quad (7)$$

Examples of SEDs obtained with INT ( $i$  and  $V$ ), Spitzer (3.6 and  $4.5 \mu\text{m}$ ), SDSS ( $u$ ,  $g$ ,  $r$ ,  $i$ , and  $z$ ), and WISE ( $W_1$ ,  $W_2$ ,  $W_3$ , and  $W_4$ ) are shown in Figure 26. The remaining SEDs are shown in the Appendix. The best-fit curves are constructed for two types of dust (solid and dashed black curves for O- and C-rich LPVs, respectively). Besides the best fit for the preferred dust species, we also show the best fit for the alternative dust species. Table A1 describes the physical properties of the LPVs, which contains information such as star ID, coordinates, magnitude ( $V$ ) and error of magnitude ( $\delta V$ ) in the Harris  $V$  filter, magnitude ( $i$ ) and error of magnitude ( $\delta i$ ) in the Sloan  $i'$

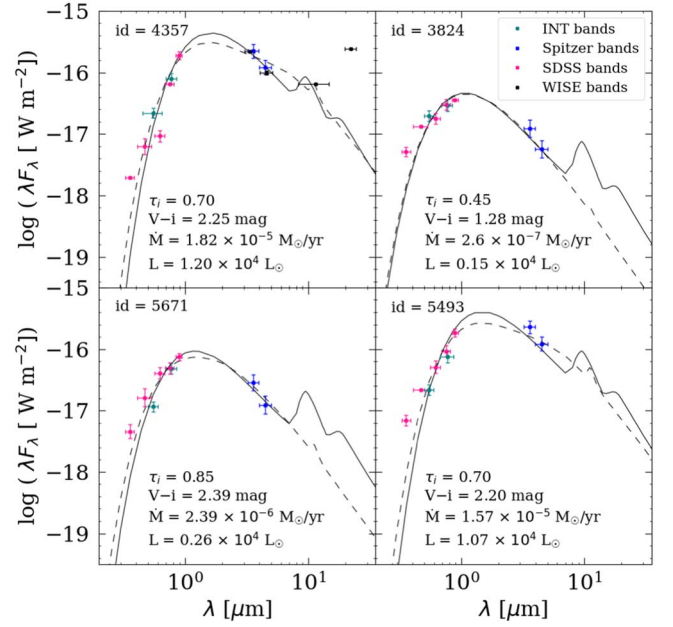


**Figure 26.** Example SEDs of LPVs with best-fit curves for the C- and O-rich AGBs (dashed and solid black lines). Fluxes are modeled by DUSTY as a function of wavelength. Fluxes observed in different bands with the INT ( $i$  and  $V$ ), Spitzer (3.6 and  $4.5 \mu\text{m}$ ), SDSS ( $u$ ,  $g$ ,  $r$ ,  $i$ , and  $z$ ), and WISE ( $W_1$ ,  $W_2$ ,  $W_3$ , and  $W_4$ ) are shown by green, blue, pink, and black squares, respectively. Vertical and horizontal error bars show photometric uncertainty in the magnitude and the difference between the  $\lambda_{\text{max}}$  and  $\lambda_{\text{min}}$  around each filter's central wavelength, respectively.

filter, amplitude in the Sloan  $i'$  filter (amplitude), birth mass ( $M_{\text{Birth}}$ ), optical depth in the Sloan  $i'$  ( $\tau_i$ ), mass-loss rate ( $\dot{M}$ ), luminosity ( $L$ ), and chemical type of LPVs.

Figure 27 shows mass-loss rates for C-rich (red squares) and O-rich (green triangles) LPVs as a function of luminosity. In order to assess the effect of the chemical types of dust on optical depth and mass-loss ratio, carbon stars were assumed to have oxygen dust (open red squares). Changing optical depth under the effect of dust species alters the mass-loss ratio and luminosity of this sample. Based on van Loon et al.'s (1999) paper, this figure shows the maximum and classical limit of mass-loss rates. The maximum mass-loss rate ridgeline is an extreme envelope of rates that were measured once in the past (van Loon et al. 1999), and given the uncertainties in those data and modeling assumptions, the actual limit may be somewhat lower; hence, we added a question mark to it. The black squares in this figure indicate Boyer et al.'s (2015b) x-AGBs with specific IDs. We have used SED modeling to estimate all four x-AGBs' mass loss (and luminosity). As shown in this figure, the two x-AGBs are mutual with the INT and Spitzer surveys, and two other of the Boyer et al. (2015b) variables were identified in the INT survey as nonvariables. This plot shows that LPVs in And IX have mass-loss rates of  $1.7 \times 10^{-7} \leq \dot{M} \leq 1.9 \times 10^{-5} M_{\odot} \text{ yr}^{-1}$  and luminosities of  $8.0 \times 10^2 \leq L \leq 1.2 \times 10^4 L_{\odot}$ . It is estimated that the mass-loss rate of the two mutual x-AGBs is about 3.6% of the total mass return rate, while if four x-AGBs were identified this rate would be 5.7%. The maximum mass-loss rate of our LPVs ( $\sim 10^{-5} M_{\odot} \text{ yr}^{-1}$ ) is around 2 dex less than the upper limit of the maximum mass-loss rates of AGBs in the LMC ( $10^{-7}$ – $10^{-3} M_{\odot} \text{ yr}^{-1}$ ; van Loon et al. 1999). In more metal-poor environments, such as in the Wolf–Lundmark–Melotte galaxy with a metallicity of  $[\text{Fe}/\text{H}] = 1.13$ , the mass-loss rate of AGBs is calculated to be

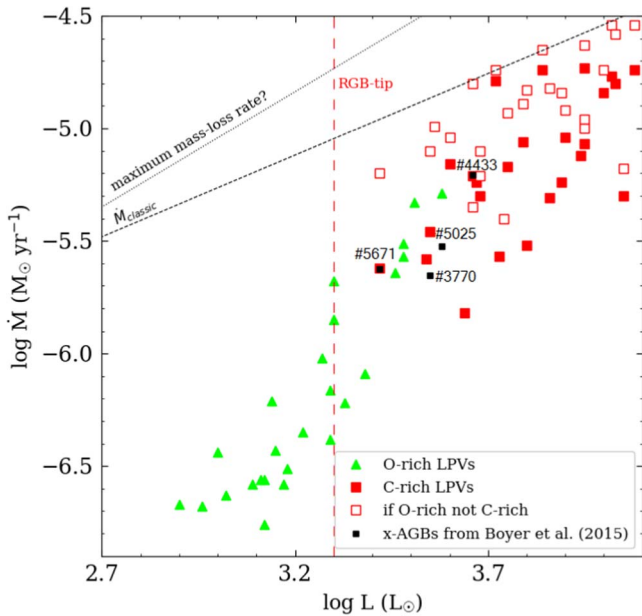


**Figure 27.** Mass-loss rate as a function of luminosity for C-rich (red squares) and O-rich (green triangles) LPVs within two half-light radii of And IX. The open red squares show the results if the carbon stars are assumed instead to be O-rich. The dotted line represents the classical single-scattering mass-loss limits  $\dot{M}_{\text{classic}} \propto L^{0.75}$ , and the mass-loss limits when multiple scattering of photons becomes important (maximum mass-loss rate?) is represented by the dashed line (van Loon et al. 1999). The tip luminosity of the RGB is marked with the red vertical dashed line. Four x-AGBs of Boyer et al. (2015b) are highlighted with their IDs, two of which are mutual in the Spitzer and INT surveys.

$10^{-10}$ – $10^{-4} M_{\odot} \text{ yr}^{-1}$  for O-rich AGBs and  $10^{-10}$ – $10^{-5} M_{\odot} \text{ yr}^{-1}$  for C-rich ones (Jackson et al. 2007).

The mass-loss rate increases during stellar evolution along the AGB phase synchronously with luminosity (and hence birth mass; Höfner & Olofsson 2018). Figure 27 illustrates the same point, as most luminous stars generally reach higher mass-loss rates. If LPVs with masses greater than  $1.5 M_{\odot}$  are assumed to be O-rich, the mass-loss rate would be higher. Due to the lower opacity of silicates compared to amorphous carbon grains, fitting carbon stars with silicates usually results in higher mass-loss rates. In this diagram, a carbon star with luminosity  $0.89 \times 10^4 L_{\odot}$  has the most mass loss,  $1.87 \times 10^{-5} M_{\odot} \text{ yr}^{-1}$ . With silicon dust, the mass loss of this star increases by 25%. As illustrated in Figure 27, mass-loss variance is evident around the RGB tip in a given luminosity (birth mass), indicating star evolution throughout the galaxy (Javadi et al. 2013). When a star climbs the AGB, its mass loss increases gradually with luminosity, allowing different mass losses to be observed at the same luminosity. Carbon stars tend to have higher luminosities and mass losses because of their higher mass; however, some carbon stars have lower luminosities ( $\log L < 3.6 L_{\odot}$  in Figure 27) and mass losses than oxygen stars. These carbon stars may be in the interthermal pulse luminosity dip and experience lower luminosity and mass-loss rate, whereas after thermal pulsation (TP) they experience higher luminosity and mass-loss rate (Vassiliadis & Wood 1993; Mattsson et al. 2007). On the other hand, the metallicity gradient in galaxies can also lead to overlaps between carbon and oxygen stars, which seem unlikely here. Even if there is a metallicity gradient in this galaxy, since we did not detect any stars in the range of 1– $1.5 M_{\odot}$ , changing this

**Table 5**

Estimations of the Mass-loss Ratios of And IX LPVs at Different Metallicities

Metallicity	$\dot{M}^a$ ( $10^{-4} M_{\odot} \text{ yr}^{-1}$ )	$\dot{M}$ ( $10^{-4} M_{\odot} \text{ yr}^{-1}$ ) (if all O-rich)	$\dot{M}/M_{\text{LPV}}^b$ ( $10^{-6} \text{ yr}^{-1}$ )	Specific Mass-loss Rate ( $10^{-10} \text{ yr}^{-1}$ )
$Z = 0.0001$	2.4	3.7	3.0	8.0
$Z = 0.0002$	1.5	2.4	2.0	6.0
$Z = 0.0003$	1.0	1.7	1.0	4.0

**Notes.**
<sup>a</sup> Total mass return rate.

<sup>b</sup> Total stellar mass of LPVs.

limit due to metallicity does not affect our results. The limit at which oxygen stars turn into carbon stars is affected by metallicity. Oxygen stars with higher mass loss and luminosity than carbon stars have spent more time evolving in the AGB phase; the luminosity of these carbon stars can also increase with further evolution in this phase (Marigo et al. 2008).

The results of the total mass return rate and the ratio of the total mass return to the total stellar mass at three different metallicities are summarized in Table 5. Moreover, we estimate the ratio of the total mass return rate to the total stellar mass of LPVs. This ratio is a measure of the duration of the dominant mass-loss phase, or rather the inverse of it. In fact, it sets an upper limit to the duration, as the stars do not completely vanish but leave remnants (white dwarfs, neutron stars, or black holes). With  $Z = 0.0001$ , the timescale is  $3.0 \times 10^5 \text{ yr}$ , which is a few times shorter than the radial-pulsation-phase timescale of  $\sim 10^6 \text{ yr}$  as predicted by models (Saremi et al. 2021). Based on this, the more extreme phase of the LPV and heavy mass loss seems to last for a shorter period of time than the whole TP-AGB lifetime. Also, we estimated the specific mass-loss rate as the total mass return by the total stellar mass in each metallicity. It is estimated that the mass loss of LPVs in about a billion years could enrich the ISM and revive star formation in the galaxy. Despite this, the mass of the ISM may be impacted by interaction with the M31 galaxy. We can refer to Buck et al.’s (2019) simulation for more information on the possibility of mass loss in satellites in the Local Group, such as And IX, via stripping. Based on this simulation, it was found that satellite galaxies have a lower present-day stellar mass ( $z = 0$ ) than the maximum total mass they have reached during their whole evolution. Accordingly, satellite galaxies with present-day stellar masses of order  $\sim 10^6 M_{\odot}$  had a maximum stellar mass of order  $\sim 10^9 M_{\odot}$  (Buck et al. 2019).

The total stellar mass and the total mass return rate in And IX decrease with increasing metallicity; the specific mass-loss rate follows this pattern. C-rich and O-rich LPVs have total mass-loss rates of  $2.1 \times 10^{-4} M_{\odot} \text{ yr}^{-1}$  and  $2.9 \times 10^{-5} M_{\odot} \text{ yr}^{-1}$  at  $Z = 0.0001$ , respectively. As carbon stars account for about 80% of the total mass return rate in the three metallicities, most of the dust that enters the ISM by LPVs is carbon dust.

## 8. Summary

From 2015 June 21 to 2017 October 6, nine observations were undertaken to study the properties of And IX, a dSph satellite of M31. Observations were conducted using the 2.5 m WFC of the INT with the Sloan  $i'$  and Harris  $V$  filters. We detected 54 AGB candidates within two half-light radii ( $\sim 5'$ ) of And IX by employing DAOPHOT/ALLSTAR



software (Stetson 1987, 1990, 1996). About 50 of them are LPVs with amplitude<sub>*i*</sub> > 0.2 mag. We calculated the SFRs as a galaxy evolution tracer in two half-light radii for metallicities of  $Z = 0.0001, 0.0002,$  and  $0.0003$ . Due to temperature and radius variations, LPVs experience significant mass loss in the form of stellar wind. We measure mass-loss rates using multiwavelength data from INT, Spitzer, SDSS, and WISE. Our primary conclusions are as follows:

1. The maximum rate of star formation  $\sim 8.2 \pm 3.1 \times 10^{-4} M_{\odot} \text{ yr}^{-1}$  occurred 6 Gyr ago at  $Z = 0.0001$ . Compared to the peak of the SFR in the more metal-rich estimation ( $\sim 5.2 \pm 2.0 \times 10^{-4} M_{\odot} \text{ yr}^{-1}$  at 5.7 Gyr ago), the peak of the SFR in the more metal-poor estimation is 57% higher.
2. The total stellar mass is estimated to be  $\sim 3.0 \times 10^5 M_{\odot}$  ( $Z = 0.0001$ ), which decreases to  $2.3 \times 10^5 M_{\odot}$  by increasing metallicity to  $Z = 0.0003$ . Furthermore, based on And IX's cumulative SFH, 90% of its total stellar mass was formed by  $\sim 3.65^{+0.13}_{-1.52}$  Gyr ago at  $Z = 0.0001$ , indicating that this galaxy had an extended SFH. Furthermore, half of the mass of And IX was formed about  $7.02^{+0.39}_{-0.56}$  Gyr ago in the more metal-poor estimation. Consequently, our results imply that this dSph satellite was quenched late, possibly due to late infall.
3. And IX shows a late epoch of star formation, peaking around 630 Myr ago, but its SFR is low, at  $1.1 \pm 0.4 \times 10^{-4} M_{\odot} \text{ yr}^{-1}$ . In this quenched galaxy, dusty stellar winds at earlier times may have contributed to this late epoch of star formation.
4. According to the different age gradients of the populations in the inner and outer parts of the galaxy, an outside-in star formation scenario could be its galaxy evolution scenario. Furthermore, the separation of population ages might have resulted from stars migrating outward after forming in the more central regions.
5. We estimated the mass-loss rate of LPVs ( $10^{-7}$ – $10^{-5} M_{\odot} \text{ yr}^{-1}$ ) by employing the DUSTY code (Ivezic & Elitzur 1997). We have shown a correlation between mass-loss rates and luminosity for AGB stars. However, there is also an evolution term for stars of a given mass that should be considered. In addition, the carbon stars

contribute much to the replenishment of the ISM with a timescale of  $\sim 3.0 \times 10^5$  yr, a few times shorter than the TP-AGB duration. Also, we calculated the total rate of mass returned to the ISM by LPVs  $\sim 1.0$ – $2.4 \times 10^{-4} M_{\odot} \text{ yr}^{-1}$  depending on the adopted metallicity. Mass loss from the LPVs could enrich the ISM in about a billion years if external or internal processes do not remove the gas.

The observing time for this survey was provided by the Iranian National Observatory (INO) and the UK-PATT allocation of time to programs I/2016B/09 and I/2017B/04 (PI: J. van Loon). We thank the INO and the School of Astronomy (IPM) for financial support of this project. H.A. is grateful to Peter Stetson for sharing his photometry routines. E.S. acknowledges financial support from the State Research Agency (AEI-MCINN) of the Spanish Ministry of Science and Innovation under the grant "The structure and evolution of galaxies and their central regions" with reference PID2019-105602GB-I00/10.13039/501100011033, from the ACIISI, Consejería de Economía, Conocimiento y Empleo del Gobierno de Canarias, and the European Regional Development Fund (ERDF) under grant with reference PROID2021010044, and from IAC project P/300724, financed by the Ministry of Science and Innovation, through the State Budget, and by the Canary Islands Department of Economy, Knowledge and Employment, through the Regional Budget of the Autonomous Community. We thank Alireza Molaeinezhad, Arash Danesh, Mojtaba Raouf, Ghassem Gozaliasl, James Bamber, Philip Short, Lucia Suárez-Andrés, and Rosa Clavero for their help with the observations.

## Appendix Supplementary Material

The Appendix includes Table A1, which provides information on variable stars such as their IDs, coordinates in R.A. and decl., magnitudes in the *V* and *i* bands along with their associated errors, *i*-band amplitude, birth mass, optical depth, mass-loss rate, luminosity, and chemical type. Additionally, Figure A1 displays the SEDs of LPV stars along with the best fit for C- and O-rich AGBs.

**Table A1**  
Characterization of Variable Candidates

ID	R.A. (J2000)	Decl. (J2000)	$V$ (mag)	$\delta V$ (mag)	$i$ (mag)	$\delta i$ (mag)	Amplitude $_i$ (mag)	$M_{\text{Birth}}$ ( $M_{\odot}$ )	$\tau_i$	$\dot{M}$ ( $10^{-6} M_{\odot} \text{ yr}^{-1}$ )	$L$ ( $10^4 L_{\odot}$ )	Chemical Type
4957	00 52 40.39	+43 06 37.20	23.26	0.08	22.68	0.06	0.56	0.95	0.30	2.11	0.19	O
2686	00 53 25.47	+43 15 19.35	21.35	0.03	20.77	0.01	0.32	1.73	0.13	7.61	0.88	C
4837	00 52 49.79	+43 10 51.66	21.89	0.02	21.29	0.04	0.30	0.93	0.25	1.42	0.19	O
4799	00 52 49.13	+43 13 21.94	21.93	0.03	21.32	0.02	0.30	0.97	0.20	5.09	0.38	O
4601	00 53 18.14	+43 15 05.66	22.34	0.03	21.70	0.01	0.64	0.80	0.36	0.17	0.13	O
3543	00 53 13.45	+43 13 31.77	22.91	0.08	22.27	0.07	0.67	0.89	0.48	0.37	0.10	O
3481	00 52 13.34	+43 13 02.46	21.40	0.03	20.70	0.01	0.29	2.10	0.38	9.06	0.79	C
4973	00 52 52.45	+43 11 18.77	22.22	0.06	21.44	0.01	0.32	0.87	0.60	0.37	0.14	O
4901	00 53 11.49	+43 16 21.95	22.56	0.07	21.77	0.03	0.54	0.83	0.50	0.31	0.15	O
4448	00 52 55.29	+43 10 27.09	21.99	0.03	21.20	0.00	0.51	2.10	0.22	8.71	0.62	C
4190	00 52 33.54	+43 12 17.17	21.60	0.01	20.77	0.00	0.72	2.90	0.34	18.74	0.89	C
3798	00 52 48.01	+43 07 33.08	21.35	0.01	20.50	0.02	0.65	1.53	0.15	1.53	0.43	C
6338	00 52 46.09	+43 09 05.12	21.90	0.02	21.02	0.03	1.11	0.93	0.40	0.81	0.24	O
3236	00 52 36.14	+43 10 11.38	21.74	0.09	20.85	0.04	0.29	1.72	0.20	5.73	0.47	C
4757	00 53 00.79	+43 10 03.84	22.11	0.02	21.16	0.04	1.30	0.97	0.65	4.69	0.32	O
3919	00 53 23.70	+43 14 25.45	21.56	0.07	20.61	0.01	0.43	1.91	0.28	8.57	0.89	C
4951	00 52 39.94	+43 09 55.47	22.15	0.05	21.20	0.05	0.41	0.93	0.51	0.95	0.19	O
5284	00 52 59.36	+43 12 04.35	22.32	0.06	21.36	0.05	0.56	0.93	0.65	0.70	0.19	O
5073	00 53 29.77	+43 09 25.70	22.67	0.04	21.69	0.03	1.01	0.81	0.66	0.28	0.13	O
4770	00 52 53.68	+43 13 41.74	22.33	0.07	21.33	0.04	1.07	0.81	0.60	0.23	0.10	O
4435	00 52 54.35	+43 13 43.06	22.33	0.06	21.33	0.03	1.20	0.95	0.65	2.30	0.29	O
4127	00 52 34.93	+43 11 22.88	21.81	0.01	20.80	0.01	0.82	2.10	0.52	5.01	0.48	C
4250	00 53 00.93	+43 11 21.29	22.15	0.07	21.14	0.05	0.91	1.53	0.14	2.68	0.54	C
4512	00 52 59.41	+43 10 35.64	22.27	0.04	21.16	0.04	1.22	0.91	0.66	0.60	0.21	O
5339	00 53 01.96	+43 09 00.93	21.56	0.06	20.42	0.01	0.62	2.20	0.29	14.56	0.99	C
4349	00 52 06.19	+43 13 30.85	21.80	0.06	20.64	0.01	0.46	0.97	0.65	3.11	0.30	O
4573	00 52 20.74	+43 09 21.40	21.91	0.06	20.75	0.02	0.32	1.93	0.37	5.72	0.77	C
3703	00 52 36.50	+43 09 43.58	22.03	0.07	20.86	0.01	1.02	2.00	0.34	6.69	0.56	C
3824	00 52 51.91	+43 12 15.05	22.72	0.04	21.44	0.06	1.12	0.83	0.45	0.26	0.15	O
3010	00 53 03.48	+43 09 08.18	21.76	0.03	20.40	0.02	0.68	1.70	0.35	4.85	0.72	C
5503	00 52 14.24	+43 08 31.38	21.85	0.01	20.50	0.01	0.40	1.90	0.55	5.01	1.12	C
3416	00 52 10.98	+43 13 22.30	22.15	0.05	20.71	0.05	0.22	1.50	0.41	2.65	0.35	C
3587	00 52 23.64	+43 08 45.66	22.16	0.01	20.71	0.04	1.14	2.20	0.74	16.41	0.52	C
5437	00 52 54.34	+43 12 40.17	23.00	0.08	21.46	0.07	0.90	0.91	0.98	0.61	0.14	O
5325	00 52 47.61	+43 11 08.23	22.91	0.06	21.31	0.05	1.90	0.90	0.67	0.45	0.16	O
4388	00 52 45.19	+43 11 49.30	22.97	0.07	21.32	0.06	1.43	1.55	0.50	3.02	0.63	C
4381	00 53 01.70	+43 06 45.22	22.16	0.05	20.42	0.01	0.75	1.70	0.50	3.49	0.35	C
4550	00 52 56.15	+43 12 22.27	23.31	0.09	21.57	0.07	1.32	0.85	0.99	0.27	0.13	O
5546	00 53 00.38	+43 14 10.44	23.38	0.10	21.62	0.06	0.96	0.83	0.95	0.26	0.12	O
4925	00 52 55.79	+43 12 38.16	23.30	0.07	21.49	0.06	1.72	2.80	0.70	18.26	0.69	C
4541	00 52 52.66	+43 15 12.78	23.61	0.07	21.80	0.02	1.41	0.89	0.97	0.42	0.19	O
5848	00 53 25.79	+43 10 20.78	22.18	0.01	20.35	0.00	1.31	2.60	0.60	17.04	1.04	C
5030	00 52 43.08	+43 14 32.50	23.83	0.05	21.86	0.04	1.00	2.00	1.02	0.21	0.08	C
4151	00 52 48.26	+43 08 49.87	22.98	0.01	21.00	0.01	1.23	0.83	0.67	6.90	0.40	O
3243	00 52 22.35	+43 06 58.08	23.11	0.07	20.95	0.00	1.16	0.90	0.87	2.67	0.30	O
5493	00 53 00.08	+43 07 44.17	22.63	0.06	20.42	0.02	2.20	2.20	0.70	15.67	1.07	C
4357	00 53 09.67	+43 10 44.04	22.61	0.05	20.36	0.00	1.41	2.60	0.70	18.18	1.20	C
4839	00 53 02.26	+43 14 47.48	23.89	0.06	21.59	0.01	1.62	0.83	1.20	0.21	0.09	O
5671	00 52 54.62	+43 10 01.29	23.30	0.08	20.91	0.06	1.55	1.55	0.85	2.39	0.26	C
4433	00 53 08.08	+43 15 01.26	22.91	0.06	20.36	0.04	1.76	1.82	0.87	6.16	0.46	C

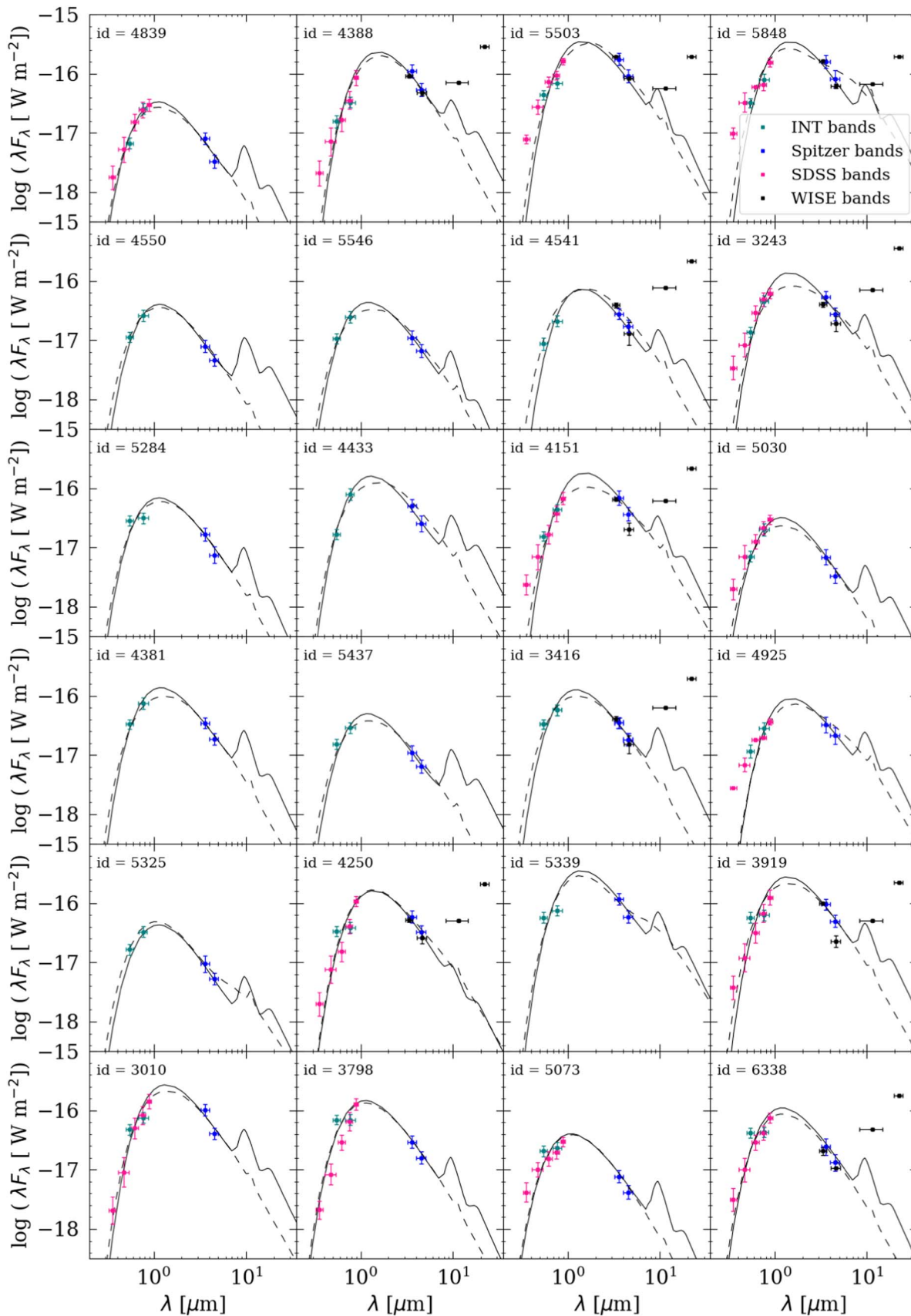


**Figure A1.** SEDs of LPVs with best-fit curves for the C- and O-rich AGBs (dashed and solid black lines). Fluxes are modeled by DUSTY as a function of wavelength. Fluxes observed in different bands with the INT (*i* and *V*), Spitzer (3.6 and 4.5  $\mu\text{m}$ ), SDSS (*u*, *g*, *r*, *i*, and *z*), and WISE ( $W_1$ ,  $W_2$ ,  $W_3$ , and  $W_4$ ) are shown by green, blue, pink, and black squares, respectively. Vertical and horizontal error bars show photometric uncertainty in the magnitude and the difference between the  $\lambda_{\text{max}}$  and  $\lambda_{\text{min}}$  around each filter's central wavelength, respectively.

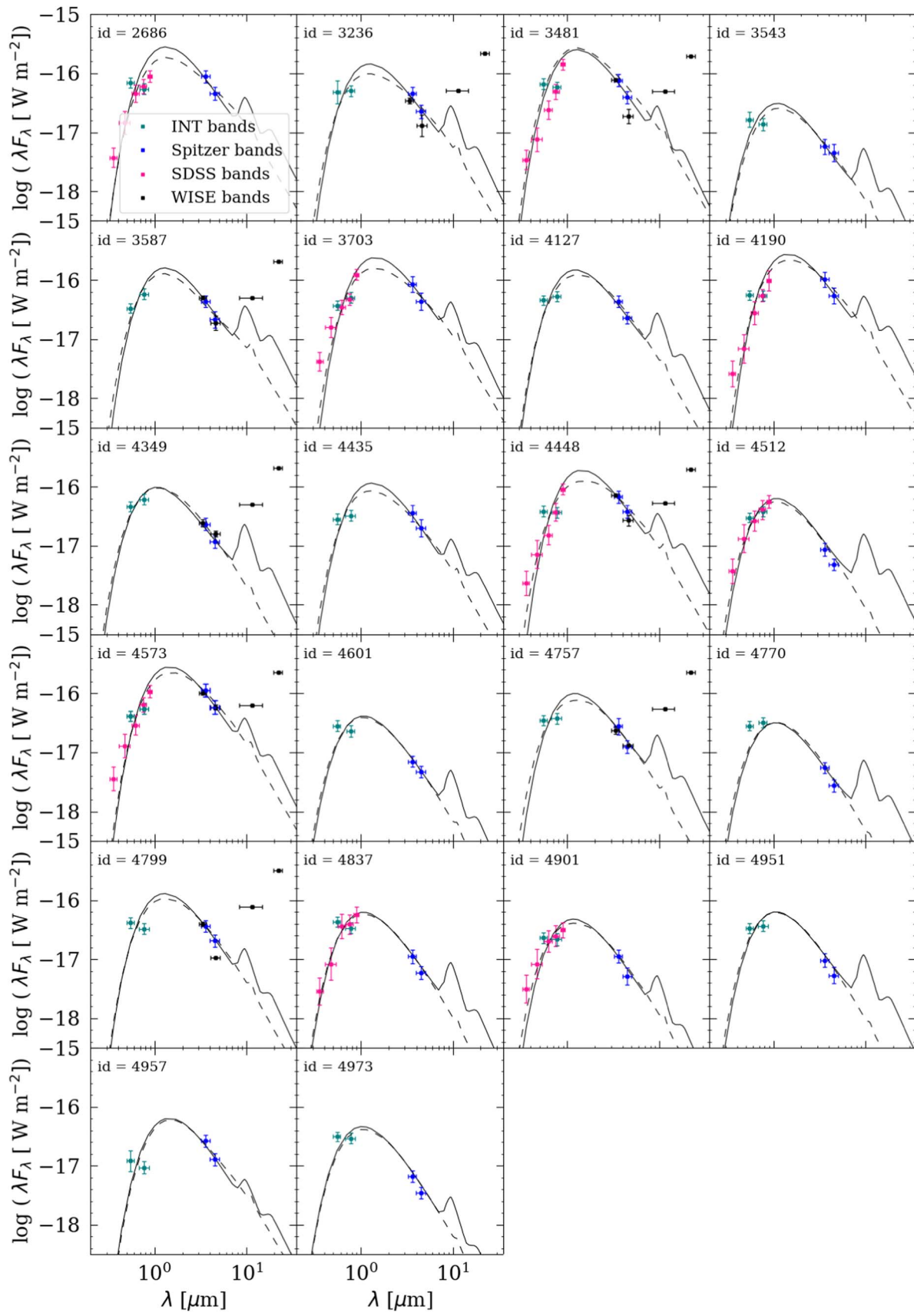










Figure A1. (Continued.)

## ORCID iDs

Hedieh Abdollahi  <https://orcid.org/0000-0002-7823-7169>  
 Atefeh Javadi  <https://orcid.org/0000-0001-8392-6754>  
 Mohammad Taghi Mirtorabi  <https://orcid.org/0000-0001-9277-3366>  
 Elham Saremi  <https://orcid.org/0000-0002-5075-1764>  
 Jacco Th. van Loon  <https://orcid.org/0000-0002-1272-3017>  
 Iain McDonald  <https://orcid.org/0000-0003-0356-0655>  
 Elahe Khalouei  <https://orcid.org/0000-0001-5098-4165>  
 Maryam Saberi  <https://orcid.org/0000-0001-7353-9101>

## References

- Applebaum, E., Brooks, A. M., Christensen, C. R., et al. 2021, *ApJ*, 906, 96  
 Battinelli, P., & Demers, S. 2013, *POBeo*, 92, 117  
 Benítez-Llambay, A., Navarro, J. F., Abadi, M. G., et al. 2016, *MNRAS*, 456, 1185  
 Boyer, M. L., Skillman, E. D., van Loon, J. T., Gehrz, R. D., & Woodward, C. E. 2009, *ApJ*, 697, 1993  
 Boyer, M. L., McQuinn, K. B. W., Barnby, P., et al. 2015a, *ApJS*, 216, 10  
 Boyer, M. L., McQuinn, K. B. W., Barnby, P., et al. 2015b, *ApJ*, 800, 51  
 Boyer, M. L., Srinivasan, S., Riebel, D., et al. 2012, *ApJ*, 748, 40  
 Boylan-Kolchin, M., Bullock, J. S., & Kaplinghat, M. 2011, *MNRAS*, 415, L40  
 Boylan-Kolchin, M., Bullock, J. S., & Kaplinghat, M. 2012, *MNRAS*, 422, 1203  
 Bressan, A., Marigo, P., Girardi, L., et al. 2012, *MNRAS*, 427, 127  
 Buck, T., Macciò, A. V., Dutton, A. A., Obreja, A., & Frings, J. 2019, *MNRAS*, 483, 1314  
 Cignoni, M., & Tosi, M. 2010, *AdAst*, 2010, 158568  
 Collins, M. L. M., Chapman, S. C., Irwin, M. J., et al. 2010, *MNRAS*, 407, 2411  
 Conn, A. R., Ibata, R. A., Lewis, G. F., et al. 2012, *ApJ*, 758, 11  
 Cutri, R. M., Wright, E. L., Conrow, T., et al. 2021, *yCat*, II/328  
 Del Popolo, A., & Le Delliou, M. 2017, *Galax*, 5, 17  
 Draine, B. T., & Lee, H. M. 1984, *ApJ*, 285, 89  
 D'Souza, R., & Bell, E. F. 2021, *MNRAS*, 504, 5270  
 Fillingham, S. P., Cooper, M. C., Kelly, T., et al. 2019, *arXiv:1906.04180*  
 Gaia Collaboration, Brown, A. G. A., Vallenari, A., et al. 2021, *A&A*, 649, A1  
 Gail, H. P., & Sedlmayr, E. 1999, *A&A*, 347, 594  
 Girardi, L., Groenewegen, M. A. T., Hatziminaoglou, E., & da Costa, L. 2005, *A&A*, 436, 895  
 Girardi, L., & Marigo, P. 2007, *A&A*, 462, 237  
 Gnedin, N. Y. 2014, *ApJ*, 793, 29  
 Goldman, S. R., Boyer, M. L., McQuinn, K. B. W., et al. 2019, *ApJ*, 877, 49  
 Goldman, S. R., van Loon, J. T., Zijlstra, A. A., et al. 2017, *MNRAS*, 465, 403  
 Hamedani Golshan, R., Javadi, A., van Loon, J. T., Khosroshahi, H., & Saremi, E. 2017, *MNRAS*, 466, 1764  
 Hanner, M. S. 1988, *Infrared Observations of Comets Halley and Wilson and Properties of the Grains* 19890003959 NASA  
 Harbeck, D., Gallagher, J. S., Grebel, E. K., Koch, A., & Zucker, D. B. 2005, *ApJ*, 623, 159  
 Hashemi, S. A., Javadi, A., & van Loon, J. T. 2019, *MNRAS*, 483, 4751  
 Hidalgo, S. L., Aparicio, A., & Gallart, C. 2008, *AJ*, 136, 2332  
 Hidalgo, S. L., Monelli, M., Aparicio, A., et al. 2013, *ApJ*, 778, 103  
 Höfner, S., & Olofsson, H. 2018, *A&ARv*, 26, 1  
 Ivezić, Z., & Elitzur, M. 1997, *MNRAS*, 287, 799  
 Jackson, D. C., Skillman, E. D., Gehrz, R. D., Polomski, E., & Woodward, C. E. 2007, *ApJ*, 656, 818  
 Javadi, A., Saberi, M., van Loon, J. T., et al. 2015, *MNRAS*, 447, 3973  
 Javadi, A., van Loon, J. T., Khosroshahi, H., & Mirtorabi, M. T. 2013, *MNRAS*, 432, 2824  
 Javadi, A., van Loon, J. T., Khosroshahi, H. G., et al. 2017, *MNRAS*, 464, 2103  
 Javadi, A., van Loon, J. T., & Mirtorabi, M. T. 2011a, *MNRAS*, 411, 263  
 Javadi, A., van Loon, J. T., & Mirtorabi, M. T. 2011b, *MNRAS*, 414, 3394  
 Jordi, K., Grebel, E. K., & Ammon, K. 2006, *A&A*, 460, 339  
 Kirby, E. N., Cohen, J. G., Guhathakurta, P., et al. 2013, *ApJ*, 779, 102  
 Klypin, A., Kravtsov, A. V., Valenzuela, O., & Prada, F. 1999, *ApJ*, 522, 82  
 Kroupa, P. 2001, *MNRAS*, 322, 231  
 Ledinauskas, E., & Zubovas, K. 2020, *MNRAS*, 493, 638  
 Lee, M. G., Freedman, W. L., & Madore, B. F. 1993, *ApJ*, 417, 553  
 Leisenring, J. M., Kemper, F., & Sloan, G. C. 2008, *ApJ*, 681, 1557  
 Marigo, P., Girardi, L., Bressan, A., et al. 2008, *A&A*, 482, 883  
 Marigo, P., Girardi, L., Bressan, A., et al. 2017, *ApJ*, 835, 77  
 Mattsson, L., Höfner, S., & Herwig, F. 2007, *A&A*, 470, 339  
 McConnachie, A. W. 2012, *AJ*, 144, 4  
 McConnachie, A. W., Irwin, M. J., Ferguson, A. M. N., et al. 2004, *MNRAS*, 350, 243  
 McConnachie, A. W., Irwin, M. J., Ferguson, A. M. N., et al. 2005, *MNRAS*, 356, 979  
 McDonald, I., & Trabucchi, M. 2019, *MNRAS*, 484, 4678  
 McDonald, I., White, J. R., Zijlstra, A. A., et al. 2012, *MNRAS*, 427, 2647  
 McDonald, I., & Zijlstra, A. A. 2016, *ApJL*, 823, L38  
 Müller, O., Fahrion, K., Rejkuba, M., et al. 2021, *A&A*, 645, A92  
 Navabi, M., Saremi, E., Javadi, A., et al. 2021, *ApJ*, 910, 127  
 Navarro, J. F. 2018, in *IAU Symp. 344, Dwarf Galaxies: From the Deep Universe to the Present*, ed. K. B. McQuinn & S. Stierwalt (Cambridge: Cambridge Univ. Press), 455  
 Nenkova, M., Ivezić, Z., & Elitzur, M. 1999, in *LPI Contributions 969, Thermal Emission Spectroscopy and Analysis of Dust, Disks, and Regoliths*, ed. A. Sprague (Houston, TX: Lunar and Planetary Institute), 20  
 Parto, T., Dehghani, S., Javadi, A., et al. 2023, *ApJ*, 942, 33  
 Pégori, B. 1988, *A&A*, 194, 335  
 Planck Collaboration, Ade, P. A. R., Aghanim, N., et al. 2014, *A&A*, 571, A16  
 Ren, T., Jiang, B., Ren, Y., & Yang, M. 2022, *Univ*, 8, 465  
 Rezaeikh, S., Javadi, A., Khosroshahi, H., & van Loon, J. T. 2014, *MNRAS*, 445, 2214  
 Rocha, M., Peter, A. H. G., & Bullock, J. 2012, *MNRAS*, 425, 231  
 Rocha-Pinto, H. J., Majewski, S. R., Skrutskie, M. F., Crane, J. D., & Patterson, R. J. 2004, *ApJ*, 615, 732  
 Rosenfield, P., et al. 2014, *ApJ*, 790, 22  
 Sakai, S., Madore, B. F., & Freedman, W. L. 1996, *ApJ*, 461, 713  
 Saremi, E., Javadi, A., Navabi, M., et al. 2021, *ApJ*, 923, 164  
 Saremi, E., Javadi, A., van Loon, J. T., et al. 2020, *ApJ*, 894, 135  
 Schlafly, E. F., & Finkbeiner, D. P. 2011, *ApJ*, 737, 103  
 Schlegel, D. J., Finkbeiner, D. P., & Davis, M. 1998, *ApJ*, 500, 525  
 Shi, J., Wang, H., Mo, H., et al. 2020, *ApJ*, 893, 139  
 Simha, V., Weinberg, D. H., Conroy, C., et al. 2014, *arXiv:1404.0402*  
 Simpson, C. M., Grand, R. J. J., Gómez, F. A., et al. 2018, *MNRAS*, 478, 548  
 Stetson, P. B. 1987, *PASP*, 99, 191  
 Stetson, P. B. 1990, *PASP*, 102, 932  
 Stetson, P. B. 1994, *PASP*, 106, 250  
 Stetson, P. B. 1996, *PASP*, 108, 851  
 Tollerud, E. J., Beaton, R. L., Geha, M. C., et al. 2012, *ApJ*, 752, 45  
 Tolstoy, E. 2003, *Ap&SS*, 284, 579  
 Valiante, R., Schneider, R., Bianchi, S., & Andersen, A. C. 2009, *MNRAS*, 397, 1661  
 van Loon, J. T., Cioni, M. R. L., Zijlstra, A. A., & Loup, C. 2005a, *A&A*, 438, 273  
 van Loon, J. T., Marshall, J. R., & Zijlstra, A. A. 2005b, *A&A*, 442, 597  
 van Loon, J. T., Cohen, M., Oliveira, J. M., et al. 2008, *A&A*, 487, 1055  
 van Loon, J. T., Groenewegen, M. A. T., de Koter, A., et al. 1999, *A&A*, 351, 559  
 Vassiliadis, E., & Wood, P. R. 1993, *ApJ*, 413, 641  
 Weisz, D. R., Dolphin, A. E., Skillman, E. D., et al. 2014, *ApJ*, 789, 147  
 Weisz, D. R., Dolphin, A. E., Martin, N. F., et al. 2019a, *MNRAS*, 489, 763  
 Weisz, D. R., Dolphin, A. E., Martin, N. F., et al. 2019b, *ApJL*, 885, L8  
 Welch, D. L., & Stetson, P. B. 1993, *AJ*, 105, 1813  
 Wetzell, A. R., Tollerud, E. J., & Weisz, D. R. 2015, *ApJL*, 808, L27  
 Wheeler, C., Hopkins, P. F., Pace, A. B., et al. 2019, *MNRAS*, 490, 4447  
 Whitelock, P., Feast, M., & Catchpole, R. 1991, *MNRAS*, 248, 276  
 Whitelock, P. A., Feast, M. W., van Loon, J. T., & Zijlstra, A. A. 2003, *MNRAS*, 342, 86  
 Whitelock, P. A., Kasliwal, M., & Boyer, M. 2017, *EPJWC*, 152, 01009  
 Wojno, J., Gilbert, K. M., Kirby, E. N., et al. 2020, *ApJ*, 895, 78  
 Wood, P. R. 1998, *A&A*, 338, 592  
 Wood, P. R., Whiteoak, J. B., Hughes, S. M. G., et al. 1992, *ApJ*, 397, 552  
 Xu, H., Wise, J. H., Norman, M. L., Ahn, K., & O'Shea, B. W. 2016, *ApJ*, 833, 84  
 Zijlstra, A. A., Loup, C., Waters, L. B. F. M., et al. 1996, *MNRAS*, 279, 32  
 Zucker, D. B., Kniazev, A. Y., Bell, E. F., et al. 2004, *ApJL*, 612, L121